School of GeoSciences

Dissertation
for the degree of

MSc in Geographical Information Sciences

Kaixin Guo

August 2025

Statement of Copyright and Originality

I declare that this dissertation represents my own work, and that where the work of others has been used it has been duly accredited. I further declare that the length of the components of this dissertation is 4950 words for the Research Paper and 3370 words for the Technical Report.

I agree that this dissertation and associated electronic documents, web pages, data, files and computer programs can be retained by the University. YES / NO

I agree that, with the permission of my supervisor(s) or the Programme Director, these materials be made available for the purposes of preparing a publication. YES / NO

I agree that, with the permission of my supervisor(s) or the Programme Director, these materials can be used within the University of Edinburgh for continued research or teaching. YES / NO

Kaixin Guo

07/08/2025

Acknowledgements

I would like to express my gratitude to my supervisor, Professor Caroline Nichol, for her guidance and encouragement and insightful discussions through many inspiring meetings. I would like to thank Tom Wade for his help during fieldwork and data preprocessing. I would like to thank Professor John Moncrieff for helping me gaining understanding on the study site during fieldwork.

I also want to thank my family and friends for their patience, encouragement and support throughout my MSc journey.

Investigating coastal dune erosion dynamics across Lundin Links golf course using high-resolution UAV imagery

Part I - Research Paper

Abstract

Coastal dune systems are dynamic environments that provide vital natural protection against storm surges and sea level rise, yet many are experiencing accelerated erosion under growing climatic and anthropogenic pressures. This study assesses recent morphological changes in a small coastal dune system at Lundin Links, Scotland, using high resolution UAV LiDAR and UAV SfM photogrammetry datasets. The survey employed RTK-enabled drone platforms and generated precise terrain models supported by ground control points.

A comparative analysis of datasets reveals strong geometric consistency between two datasets. Given its lower cost and simplicity, photogrammetry proves sufficient for capturing small scale dune dynamics in open coastal environments. Multitemporal digital elevation models derived from UAV and historical LiDAR data, volumetric and spatial analyses show a shift from initial localised accretion to widespread erosion, with an acceleration in sediment loss after 2020. Change detection highlights crest lowering and landward retreat, raising concerns about future exposure in areas adjacent to golf course fairways.

These changes align with national coastal change trends and is likely exacerbated by recent extreme weather events. This research demonstrates the effectiveness of UAV SfM and support more frequent, accessible monitoring approaches to inform adaptive management under increasing climatic risk.

Keywords: UAV; LiDAR; Structure from motion; Photogrammetry; Coastal dune erosion

1 Introduction

1.1 Coastal dunes vulnerability

Coastal dunes are among the most dynamic landforms on the planet, playing a crucial role in protecting coastal regions from storm surges, sea-level rise, and flooding. They serve not only as natural buffers but also as ecological zones that support unique flora and fauna and provide spaces for recreation (Feagin et al., 2023; Hanley et al., 2014). However, dune morphology is shaped by complex interactions between sediment supply, wind and wave action, vegetation cover, and human land use. These systems are naturally mobile and evolve over time, making them resilient and delicate at the same time (Farrell et al., 2024).
Understanding dune vulnerability requires assessing both rapid episodic changes and long term geomorphological trends, as dunes respond differently to individual storm events compared to longer term evolution (Bakker et al., 2016). Human activities such as infrastructure development, recreation facilities, and coastal defence interventions can disturb sediment balance and vegetation structure. In many areas, coastal dunes are trapped between rising seas and fixed infrastructure, limiting their natural landward migration and exacerbating vulnerability (Silva et al., 2020). Meanwhile, climate change is amplifying the frequency and severity of extreme events such as storms and high tides that can cause rapid erosion and overwash (Pang et al., 2023; Ruessink et al., 2017). Therefore, there is growing urgency to monitor and manage dune environments to ensure both ecological resilience and the protection of coastal assets.

1.2 Golf course in Scotland

In Scotland, dune systems carry not only ecological importance but also cultural and economic significance. Scotland is the birthplace of modern golf, and many of its most iconic courses are located on coastal “links”, which means sandy, undulating terrain formed by ancient dune systems. They are found mostly along the east coast and are highly prized for their natural setting and playability. Their popularity remains high, with around 1.5 million adults in the UK playing golf weekly—twice the participation rate of tennis or badminton (Skillen et al., 2023).

For many courses, particularly traditional links, the dunes are not merely scenic features but structural elements. They offer essential protection from erosion and sea incursion, safeguarding the playing areas and surrounding infrastructure (Rennie et al., 2021; Rebanal Martínez, 2021). At the same time, the presence of golf courses brings land use challenges. Keeping the grass playable can interfere with natural dune movement, especially in areas where courses are close to fragile dunes.

The study area of this research is the Lundin Links golf course on the Fife coast. The site is directly exposed to erosive forces from the North Sea. Historical aerial imagery and topographic data indicate significant shoreline retreat in recent years, raising concerns about long-term sustainability.

1.3 Remote sensing for erosion monitoring

Accurate and repeatable monitoring of coastal dune morphology is critical for understanding patterns of erosion and sediment redistribution. Traditional ground surveys using GPS-RTK, total stations and fixed transect methods provide precise point data but are labour-intensive, spatially limited in dynamic or inaccessible environments.

Remote sensing techniques have increasingly replaced traditional approaches due to greater flexibility, efficiency, and lower cost (Pinton et al., 2023; Perko et al., 2022). Airborne LiDAR offers wide area coverage with high vertical accuracy and effective penetration through sparse dune vegetation (Donker et al., 2018; Le Mauff & Eisemann, 2022; Pinton et al., 2023), making it ideal for modelling terrain with less vegetation. However, it is often costly, less flexible in temporal resolution, and typically acquired by national agencies with long intervals. Similarly, terrestrial LiDAR, while cost effective and precise, has limited spatial coverage and is intrusive in sensitive ecosystems (Laporte-Fauret et al., 2019).

In contrast, unmanned aerial vehicles (UAV) offer a more cost effective and adaptable alternative for high resolution surface monitoring and it has been widely used for coastal areas surveying (Wang et al., 2017; Lin et al., 2019). UAVs are commonly used with LiDAR or SfM (Structure from Motion) techniques (Pinton et al., 2020). LiDAR systems utilise laser pulses to generate spatial data, enable producing exceptionally dense point clouds (Hartley et al., 2020). The high density of LiDAR generated point clouds enables precise detection of fine scale topographic variations and subtle shifts in dune morphology. SfM reconstructs 3D terrain models from overlapping imagery and ground control points, enabling sub-decimetre horizontal and vertical precision at a fraction of the cost of LiDAR based systems (Clark et al., 2023; Grottoli et al., 2021; Mancini et al., 2013; Westoby et al., 2012). For coastal dunes, UAV SfM has demonstrated point densities and topographic detail comparable to airborne LiDAR (Grohmann et al., 2020). This method involves extracting 3D spatial information by aligning and matching features across multiple overlapping 2D photographs (Gómez et al., 2015). SfM has been successfully applied in various environmental monitoring contexts, including crop mapping in agriculture (Comba et al., 2018), vegetation surveys in salt marshes (DiGiacomo et al., 2020), and coastal landscape assessments (Casella et al., 2020).

Despite growing adoption of UAV monitoring approaches, some important gaps remain. Most case studies focus on expansive natural dune systems or open beaches, while smaller, highly managed dunes like recreational beach sites are under explored. Additionally, direct comparisons between UAV LiDAR and UAV SfM photogrammetry are still limited, most existing studies evaluate one technique in isolation. This research addresses that gap by conducting a direct, high resolution comparison between UAV SfM photogrammetry and UAV LiDAR datasets over a managed dune system at Lundin Links.

1.4 Aim and objectives

1.4.1 Research aim

This study aims to assess recent morphological changes in a small coastal dune system in Scotland using UAV based LiDAR and SfM photogrammetry, comparing two datasets and identifying erosion patterns to inform future dune management.

1.4.2 Specific Objectives

O1. Collect UAV based LiDAR and photogrammetry data, compare the accuracy and suitability of the two datasets for mapping small scale coastal dune systems.
O2. Generate high resolution DEMs (digital elevation models) of the dune system using UAV LiDAR data and quantify volumetric and spatial changes between 2012 and 2025 using multitemporal LiDAR data.
O3. Identify erosion hotspots and change patterns across the site and provide recommendations for adaptive dune management in response to observed trends.

2 Methodology

2.1 Study Area

Lundin Links Golf Course is located on the southern coast of Fife, Scotland, fronting the north shore of the Firth of Forth. Established in 1868, it is a traditional Scottish links course, built directly into a narrow coastal dune system that separates the golf terrain from the sea. These foredunes form the natural coastal defence for the site, protecting fairways, footpaths, and nearby infrastructure from wave action and flooding. They are highly sensitive to both gradual processes of erosion and episodic events, including storm surges and high tides. The changing nature of the dune system and the vulnerability to extreme weather highlight the importance of morphological monitoring.

Figure 1 Study site: Lundin Links

2.2 Data Acquisition

This study utilises both publicly available data and newly acquired UAV-based datasets to assess coastal dune change at Lundin Links, Fife.

2.2.1 Public data acquisition

Public LiDAR data were obtained from the Scottish Public Sector LiDAR (*Scottish LiDAR Remote Sensing datasets | Scottish Government*): Phase 2 (2012), Phase 4 (2017), and Phase 5 (2020). Each dataset includes point clouds in compressed LAS (LiDAR Aerial Survey) format and 50 cm resolution Digital Terrain Models (DTMs), available via the Scottish Remote Sensing Portal. Coverage for 2012 was limited to the eastern portion of the site, while the 2017 and 2020 datasets provided full spatial coverage. These were used for multi-temporal analysis of morphological change.

2.2.2 UAV data acquisition

UAV data collection was conducted on 1 May 2025. The 3 flights were manually operated by Tom Wade (Airborne Geoscience) using a DJI Matrice 300 RTK (Real-Time Kinematic) platform (DJI, Shenzhen, China), equipped with two interchangeable sensors: the Zenmuse L1, a LiDAR and RGB module, and the Zenmuse P1, a 45 MP full-frame photogrammetric camera. Flights were conducted under stable weather conditions at altitudes of ~57 m AGL, with ground control provided by ten RTK-surveyed ground control points (GCPs) across the study area.

The L1 survey produced colorised point clouds with an average density of ~997 pts/m² and RGB ground sampling distance (GSD) of ~1.6 cm. The P1 survey was conducted using a 35 mm lens, capturing nadir and oblique images at ~0.7 cm GSD with 70% sidelap and 80% endlap. These datasets support high resolution 3D surface reconstruction and sensor comparison for change detection analysis.

Table 1 Flight characteristics

Parameter	L1 LiDAR Survey	P1 Photogrammetry Survey
Sensor	DJI Zenmuse L1	DJI Zenmuse P1
Imagery	LiDAR + RGB	RGB
Survey Height	57 meters AGL	57 meters AGL (35mm) / ~50m (50mm)
Ground Sample Distance	1.56 cm (RGB) / ~997 pts/m² (LiDAR)	0.72 cm (35mm) / est. <1 cm (50mm)
Flight Speed	~5 m/s	~5 m/s

2.3 Data Processing

2.3.1 GNSS Data Correction

Ground Control Points (GCPs) were surveyed using Emlid RS2+ GNSS receivers in real-time kinematic (RTK) mode. Static post-processing was performed in Emlid Studio to determine the

precise base station position, while Stop-and-Go processing was applied to refine rover-based GCP coordinates. These corrected coordinates were used to georeference both LiDAR and photogrammetric data.

2.3.2 UAV Data Processing

LiDAR and RGB data from the DJI Zenmuse L1 and P1 sensors were processed separately. LiDAR data were pre-processed in DJI Terra to generate a colorized LAS point cloud. Photogrammetric processing of the P1 imagery was carried out in Pix4Dmapper 4.6.4, including aerial triangulation, dense matching, and generation of a high-resolution point cloud, digital surface model (DSM), and orthomosaic. For clarity, this report refers to datasets derived from the Zenmuse P1 photogrammetric camera as P1, and those from the Zenmuse L1 LiDAR sensor as L1. This terminology applies to both the raw data and the processed outputs, including point clouds, models, and visualisations in the Results section.

2.3.3 Point Cloud and Surface Model Comparison

Point clouds from the L1 and P1 sensors were compared to evaluate spatial consistency and geometric differences. Iterative Closest Point (ICP) registration was used prior to comparison to minimise alignment errors:

$$E(R,t) = \frac{1}{N}\sum_{i=1}^{N} \left\| q_i - (Rp_i + t) \right\|^2$$

Where R is the rotation matrix, t is the translation vector, p_i are the source points, and q_i are the corresponding target points (Besl and McKay, 1992).

After aligning the point clouds using ICP, Cloud-to-cloud (C2C) distance was calculated in CloudCompare :

$$d_i = \min_{j \in P} \left\| p_i - p_j \right\|$$

where $p_i$is a point in the reference cloud and p_j is a point in the compared cloud (Arun et al., 1987).

2.3.4 DEM Generation

LAStools was selected for ground classification across both LiDAR and photogrammetric point clouds. The lasground_new tool implementing the Progressive TIN Densification (PTD) algorithm was used with customized parameters to retain fine terrain features while accurately classifying ground points (rapidlasso GmbH, 2018). In the following classification, lasthin was

applied to reduce point density, preserving the most representative point per 0.25 m grid cell and eliminating tile edge artifacts. After merging four photogrammetric tiles via lasmerge, only ground-classified points (class 2) were retained. Finally, las2dem converted the cleaned point cloud into a high-resolution (0.25 m) DTM.

For DSM generation, CloudCompare's Rasterize tool was employed using the maximum height option, capturing the highest visible surface, including vegetation and structural elements.

2.3.5 Volumetric Change Detection

To detect elevation change over time, historical and current DEMs were differenced using the DEM of Difference (DoD) method:

$$\mathrm{DoD} = \mathrm{DEM}_{t2} - \mathrm{DEM}_{t1}$$

where DEM_{t1} and DEM_{t2} represent terrain models from two time periods. Volume change was estimated by summing the elevation differences across all cells:

$$\Delta V = \sum (z_{t2} - z_{t1}) \cdot A_{\text{cell}}$$

where ΔV is the total volume change, z_{t1} and z_{t2} are elevation values at each time, and A_{cell} is the raster cell area (e.g., 0.5m×0.5m=0.25m², A=0.25 m² is for 0.5 m resolution).

2.3.6 Profile Analysis

Topographic profiles were extracted using profile tool in QGIS 3.34, along longitudinal and cross section transects to visualise dune morphology and assess change over time. These were used in combination with volumetric results to identify erosion hotspots and dynamic dune zones.

2.3.7 Methodological Workflow

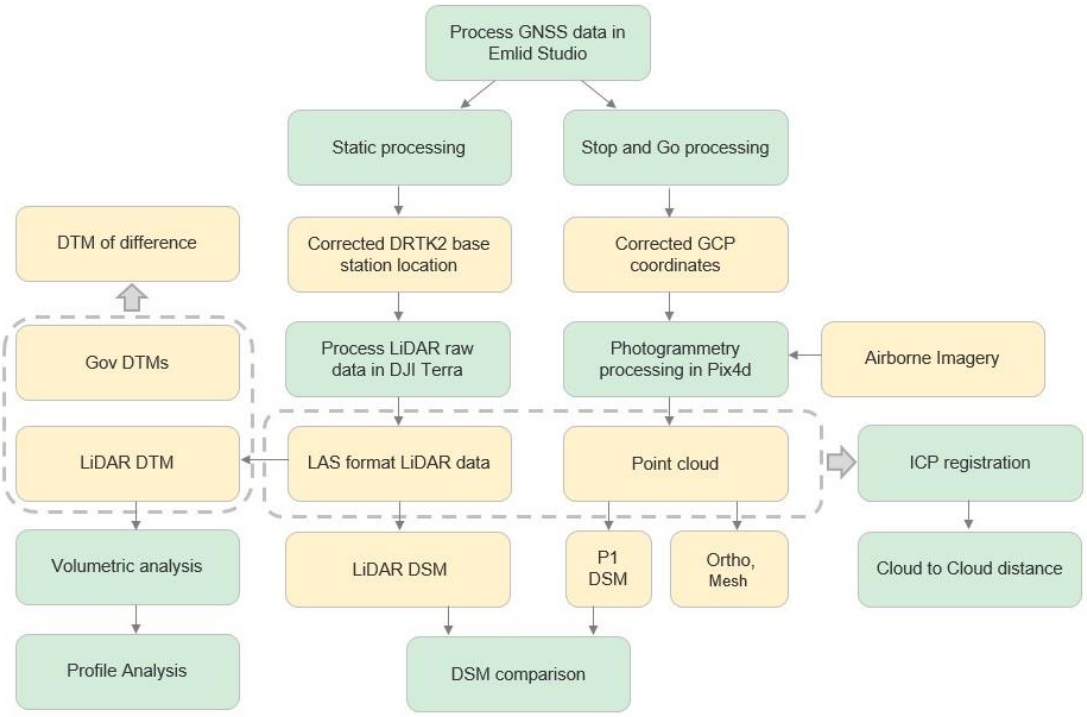

Figure 2 Methodological Workflow

3. Results

The processed RGB orthomosaic, point clouds of LiDAR and Photogrammetry are presented in Figure 3-5. Figure 6 and 7 display the result of datasets comparison. Temporal change results including DoD, volumetric analysis and profile analysis are presented in Figure 8-18.

3.1 Processed Study Site Map

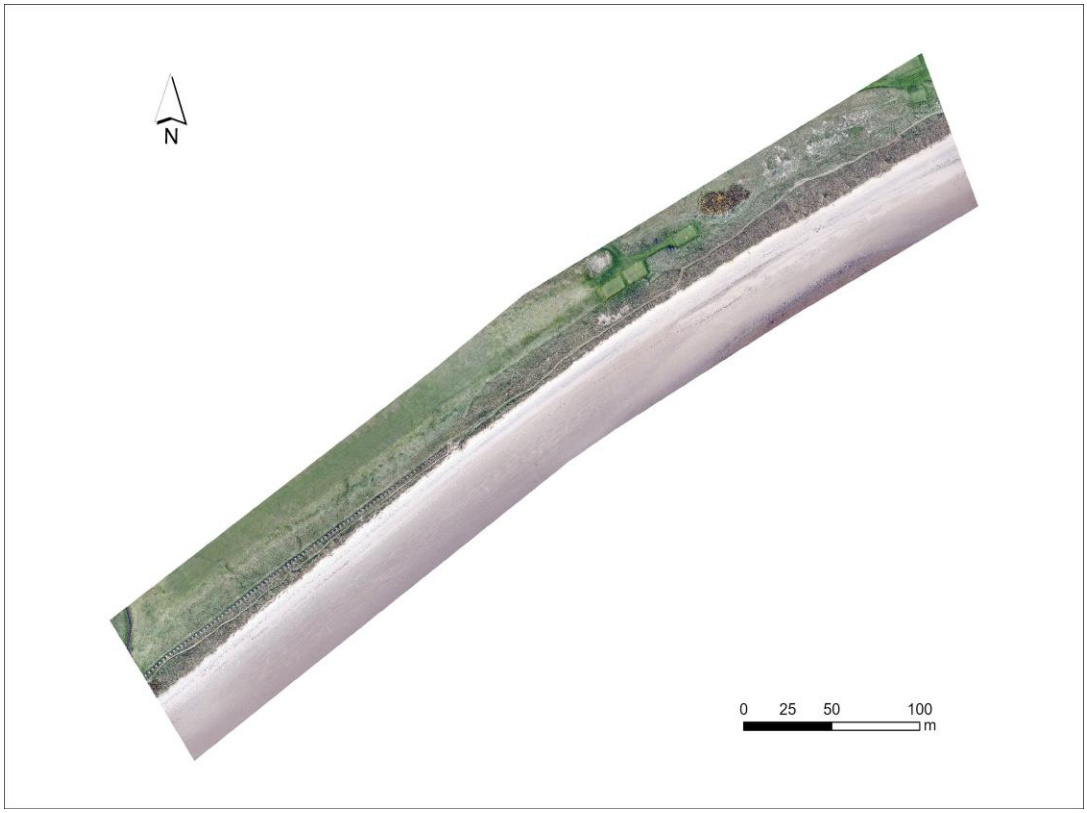

Figure 3 RGB orthomosaic processed in Pix4D

3.2 Datasets Comparison: LiDAR vs Photogrammetry

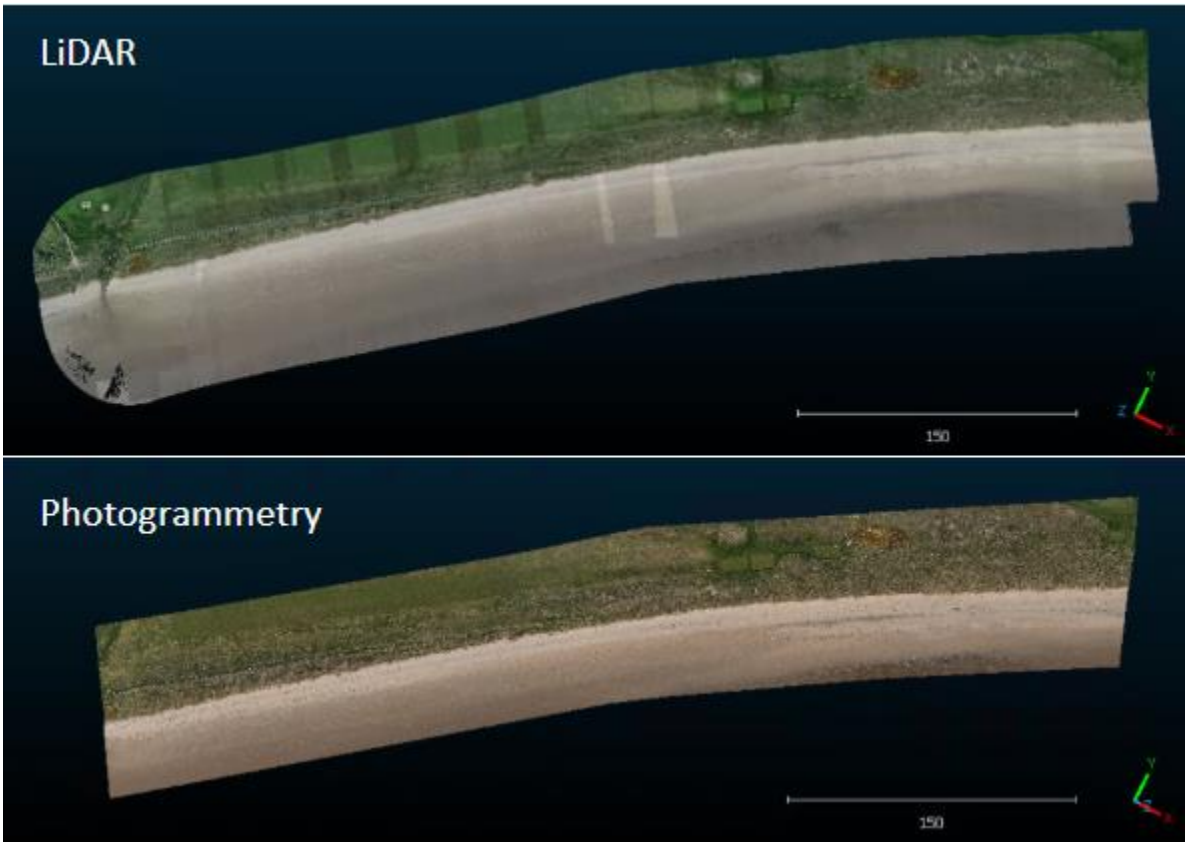

Figure 4 LiDAR and photogrammetric point clouds in CloudCompare

To examine geometric differences between the LiDAR and photogrammetric datasets, a qualitative comparison was conducted using the original coloured point clouds (Figure 4).

Figure 5 shows two representative profiles along the dune front and upper beach, captured from the same viewing perspective. The L1 point cloud exhibits consistently higher density, particularly on steep dune slopes. This enables a clearer reconstruction of microtopographic features and sharper terrain transitions. In contrast, the P1 dataset shows visibly lower point density in steep areas. The comparison shows that L1 provides a more complete and detailed 3D representation of the terrain in challenging environments, particularly where vegetation and slope affect image based reconstruction.

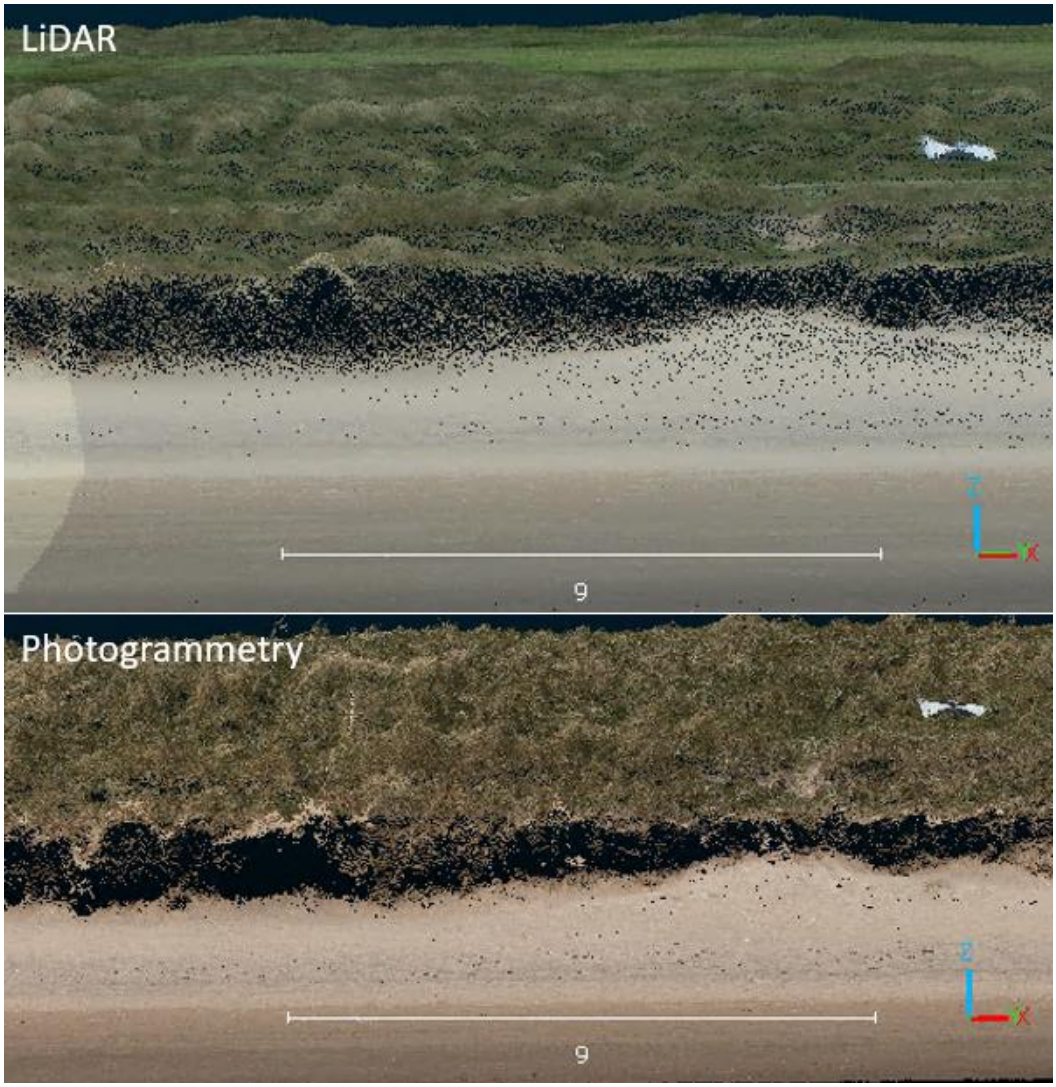

Figure 5 Point cloud of dune front showing lower density and reduced surface capture in the P1 dataset compared with the LiDAR one

Following the visual comparison of the two point clouds, a Cloud to Cloud (C2C) distance analysis was performed to quantitatively assess geometric differences and validate the observed patterns. The result of C2C distance (Figure 6) showed a strong agreement between the two point clouds. Most distances were below 0.1 m, with values ranging from 0.003 m to 1.29 m. Lower values are mainly clustered on the beach or course fairways, where both sensors produce consistent surfaces. Larger discrepancies were mostly observed in vegetated areas. However, C2C highlights only where the two clouds diverge, not in which direction.

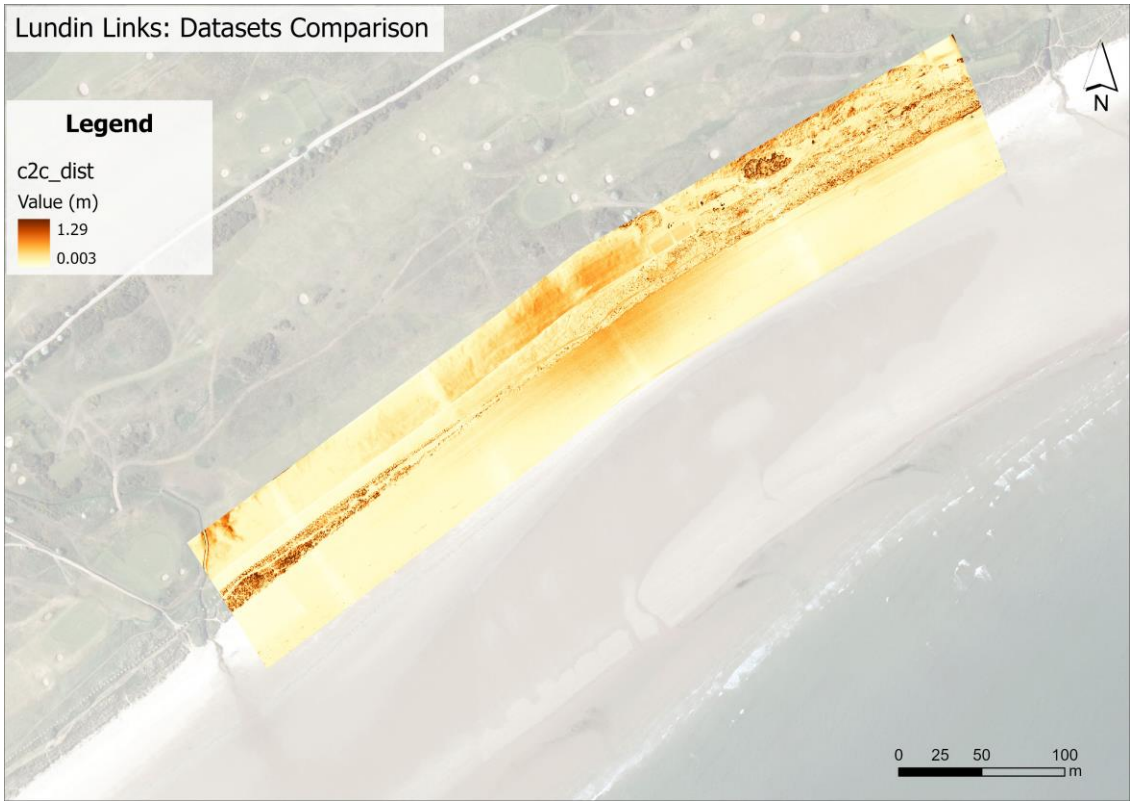

Figure 6 Cloud to cloud distance between P1 and L1 point clouds

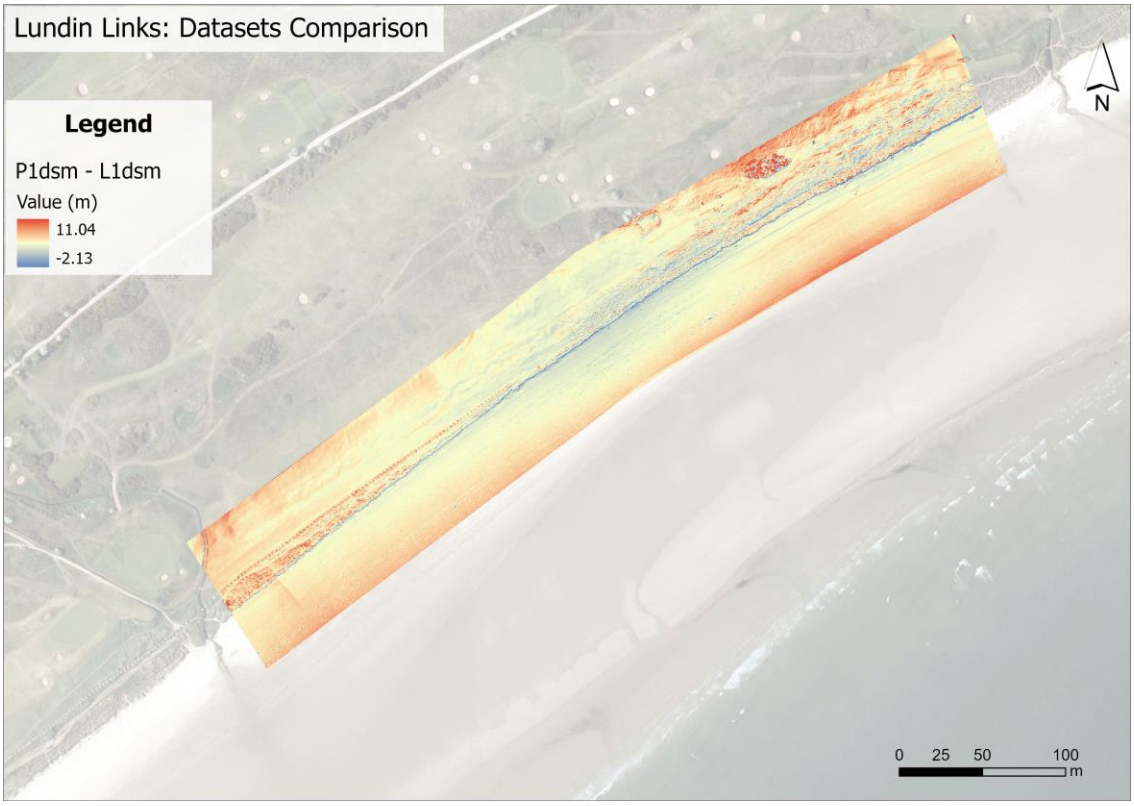

Figure 7 DSM of difference between P1 and L1 point clouds

To better assess the vertical bias, both point clouds were rasterised to 0.25 m resolution DSMs then calculated the z value difference (P1-L1) (Figure 7). The result (Table 2) revealed values ranging from -2.13 m to +11.04 m. The mean value was -0.003 m, suggesting no significant overall vertical bias between the two sensors. The standard deviation was 0.203 m, indicating that most differences were within a ±20 cm range. This value gives a good indication of the typical vertical uncertainty between the datasets.

Table 2 DSM comparison statistics

Statistics	Min	Max	Mean	Std. Dev.
Value (m)	-2.1331	11.04	-0.0029	0.2029

Large positive differences (up to +11 m) were mostly found in vegetated areas, where the photogrammetric DSM captured canopy surfaces while LiDAR sensor penetrated the canopy and represent ground surface. In contrast, large negative values (down to -2.1 m) occurred on steep dune slopes, likely where SfM photogrammetry failed to reconstruct parts of the surface but LiDAR still returned valid ground points. The DoD standard deviation (~0.20 m) can be used as a threshold to mask out noise in later erosion analyses.

The sensor comparison reveals that photogrammetry achieves adequate accuracy for coastal dune monitoring, with overall agreement demonstrated by near-zero mean difference (-0.0029m) and low standard deviation (0.2029m). While systematic differences occur in specific terrain types, the results suggest photogrammetry can provide cost-effective monitoring solutions for many coastal applications.

For temporal change analysis in the next section, LiDAR data was selected to ensure consistency with existing government datasets and enable comparison with historical records.

3.3 Temporal Change from 2012 to 2025

3.3.1 DTM of Difference (DoD) analysis

The DoD analysis across 3 time periods (2012-2017, 2017-2020 and 2020-2025) reveals distinct patterns of coastal dune evolution at the Lundin Links study site. The analysis demonstrates both erosional and accretional processes across different temporal scales and spatial zones within the dune system.

The 2012-2017 period (Figure 8) shows large areas of accretion (red zones) on the beach, with elevation gains reaching 1.0-1.2 meters. This represents significant sediment accumulation, likely driven by wind and sediment supply from the adjacent beach system. Along the dune front line, 0.5 to 1 m accretion patterns appear on the eastern most part while western part experienced -1.6 to -0.8 m loss. In the 2017-2020 period (Figure 9) the study area experienced widespread erosion (blue zones) particularly concentrated in the western portion of the dune, while the easternmost area showed a smaller portion of accretion compared with previous

period. By 2020-2025, erosional processes intensified further, with losses extending to 2.6 meters in the most affected areas (Figure 10). The extreme values are different in each map, with erosion changing from -1.6 to -2.6 while accretion from 1.2 to 1.9. The erosional zone expanded to form a more continuous band across the dune front area, indicating system-wide instability. The progression from localised accretion to widespread degradation suggests the dune system has experienced significant changes in its geomorphological evolution.
The consistent location of dune erosion along the dune face indicates that the western area represents the primary interface between marine and terrestrial processes. The intensification of dune erosion over time suggests that the natural protective capacity of the dune system is being compromised, potentially exposing inland golf course areas to increased coastal hazards.

The 2020-2025 period DoD maps of 2020 government LiDAR data with L1 (Figure 10) and P1 (Figure 11) DTM respectively show very similar results in mapping dune changes. Both datasets identify the same spatial patterns of dune erosion, with the main erosional areas clearly shown in both surveys along the dune face. The P1 system records maximum dune losses of 2.2 meters compared to 2.6 meters from L1 DTM, showing a slightly lower but highly correlated measurement approach. The spatial agreement between methods is particularly clear in the dune transition zones where stable dune areas (yellow) meet eroded dune zones (blue). This pattern consistency proves that the photogrammetric approach works well for dune monitoring while being cost-effective and accessible.

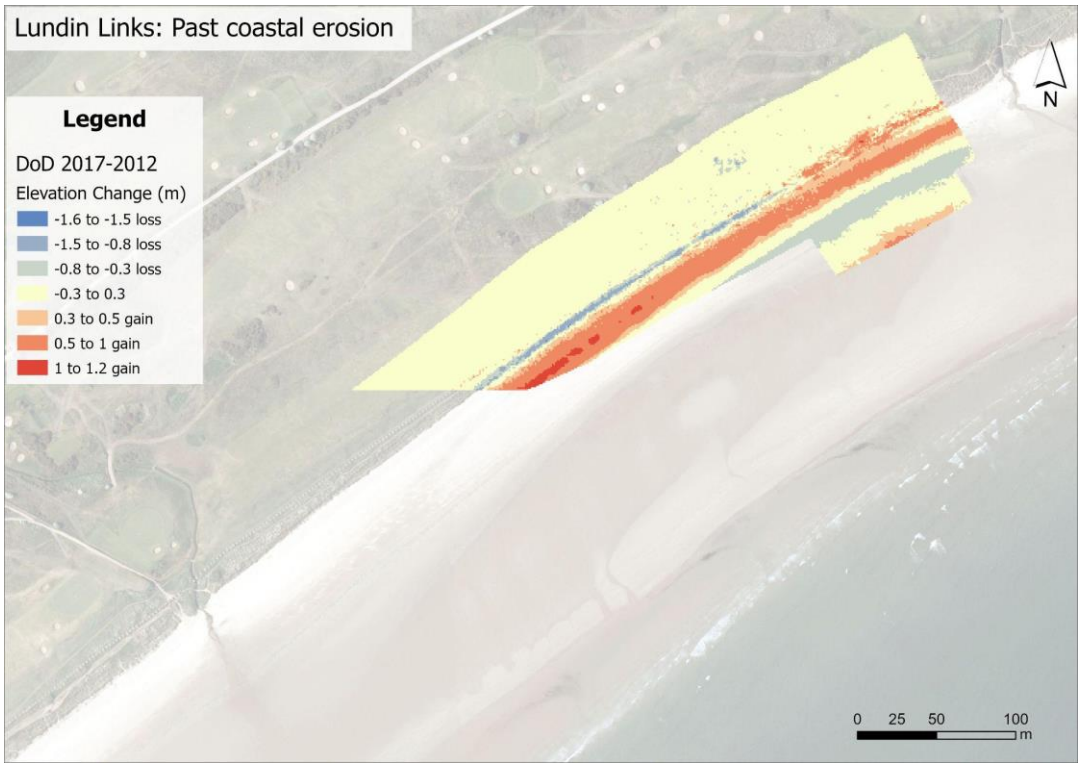

Figure 8 2012-2017 DoD

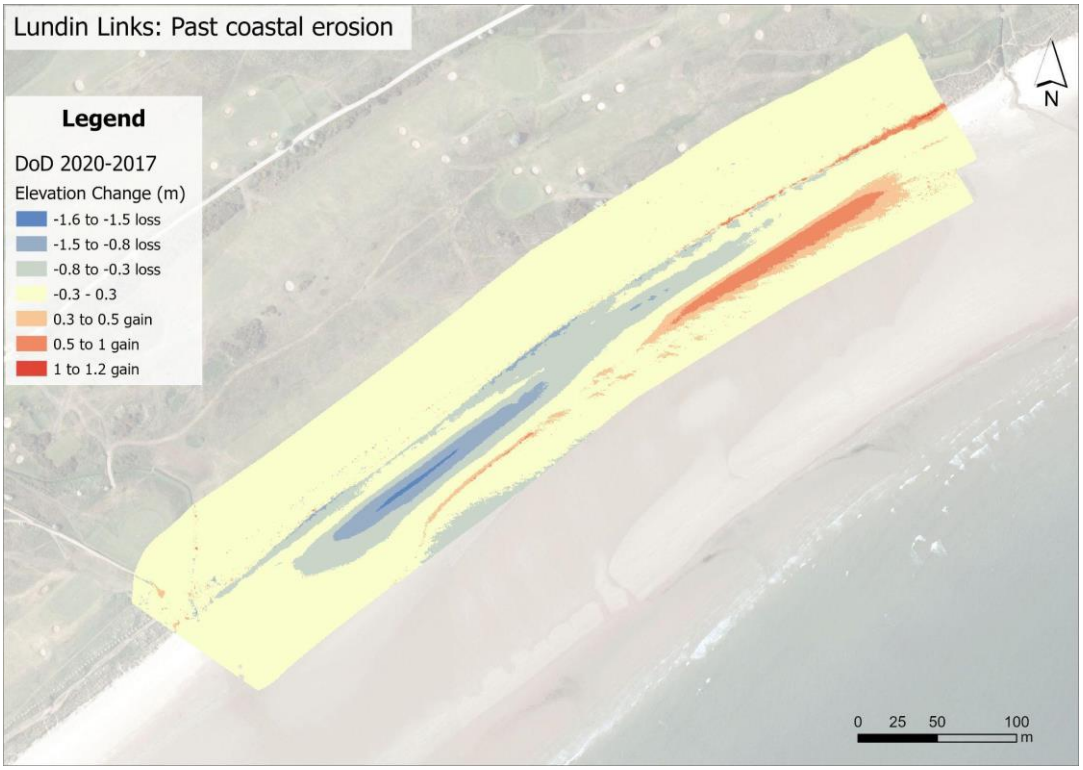

Figure 9 2017-2020 DoD

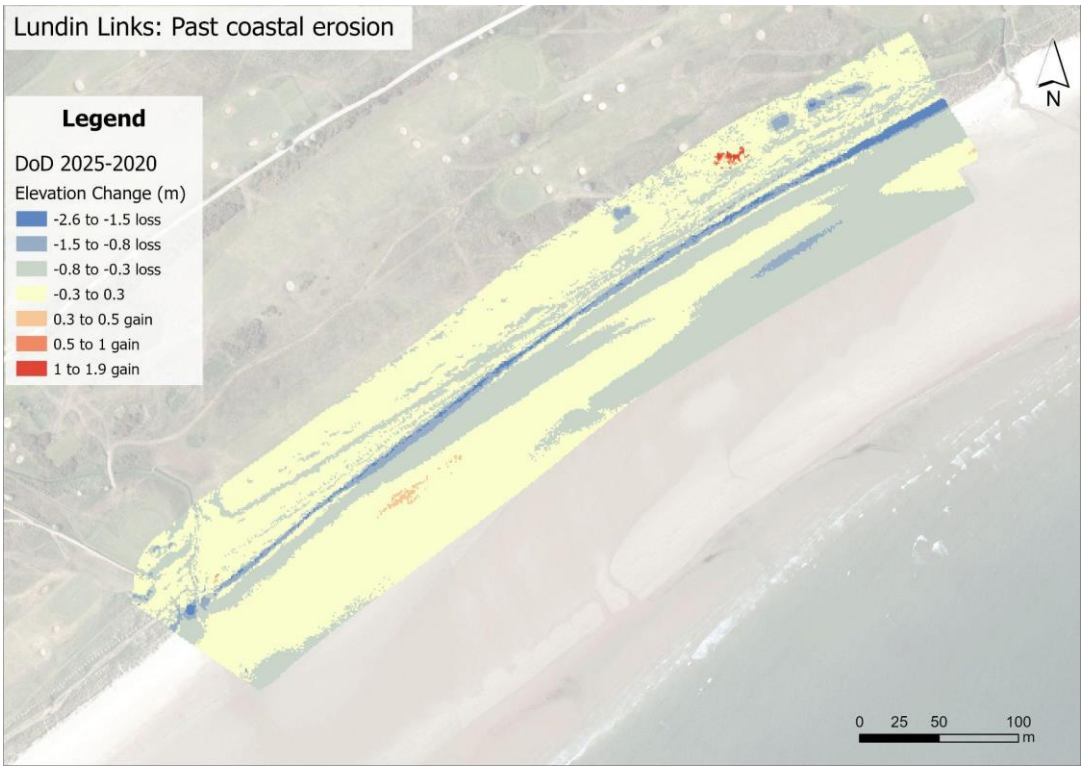

Figure 10 2020-2025 L1 and gov2020 DoD

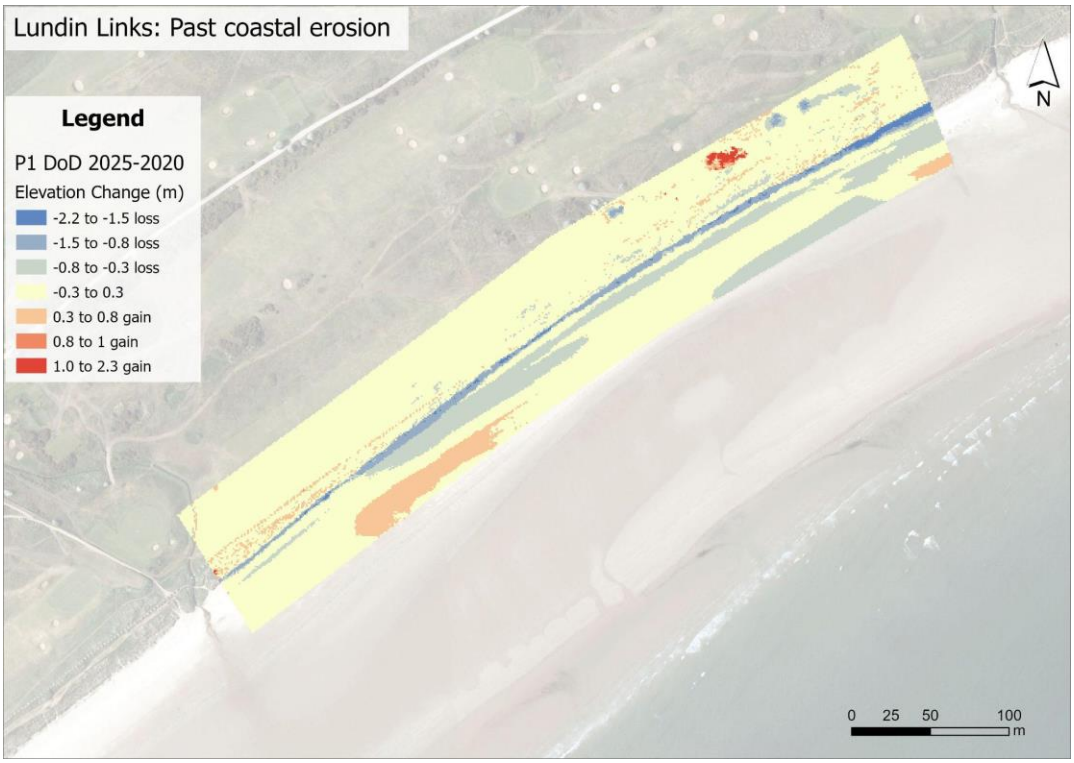

Figure 11 2020-2025 P1 and gov2020 DoD

3.3.2 Volumetric Analysis

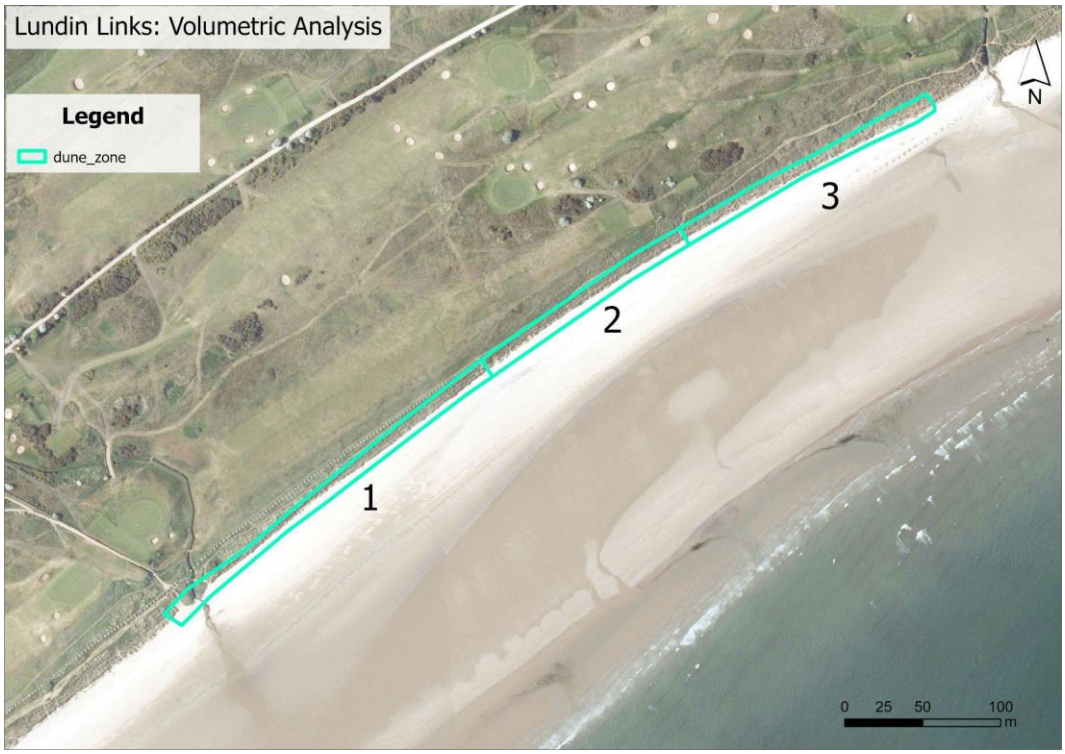

Figure 12 Three zones of the dune front

To further assess and quantify spatial variations in coastal morpho dynamics in specific parts, the dune face was classified into three distinct zones (Figure 12) based on their surface features and potential influences. Zone 1, positioned in the westernmost section, contains several WWII era concrete anti-tank blocks near the dune front, which may locally alter wave energy or sediment transport, potentially affecting erosion. Zone 2 protects some golf course fairways but no hard structures. Zone 3 is at easternmost, lacks visible infrastructure, representing a relatively undisturbed area.

The Volume Change bar chart reveals erosion patterns across the three zones (Figure 13). During 2012-2017, minimal changes occurred across all zones, with Zone 3 showing slight accretion (+420 m^3) while Zone 2 experienced modest erosion (-415 m^3). Zone 1 data was unavailable for this period.

The 2017-2020 period marked a significant shift, with substantial net erosion in Zones 1 (-1998 m^3) and 2 (-2016 m^3), while Zone 3 experienced notable accretion (+724 m^3). This pattern suggests potential sediment redistribution from the western zones toward zone 3.

The most recent period (2020-2025) demonstrated intensified erosion across all zones, with total volume losses of -2061 m^3, -1305 m^3, and -1885 m^3 for Zones 1, 2, and 3 respectively. This represents a dramatic reversal for Zone 3, transitioning from accretional to strongly erosional behaviour.

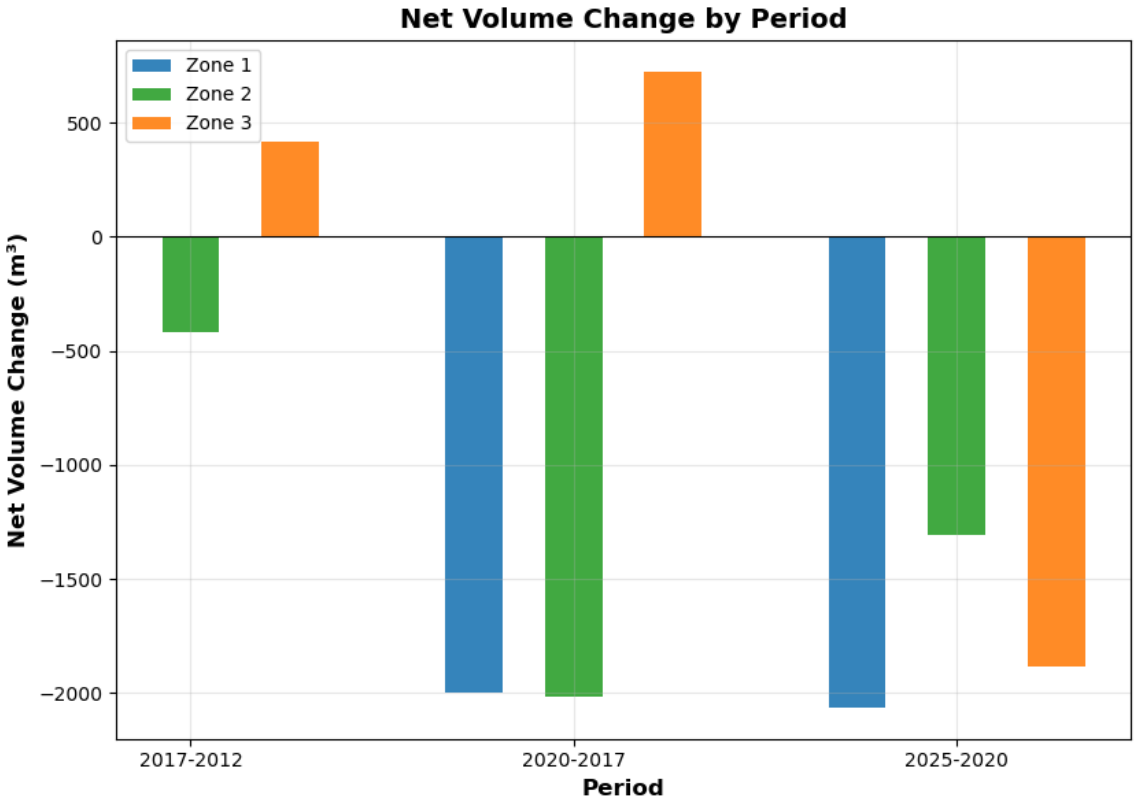

Figure 13 Volume Change bar chart

Average depth changes (Figure 14) further illustrate these patterns. Zone 1 maintained relatively consistent erosion depths (-0.71 to -0.73 m) across periods. Zone 2 experienced the most variable behaviour, with erosion depths ranging from -0.21 m to -1.01 m. Most notably, Zone 3 transitioned from accretion (+0.21 to +0.35 m) to severe erosion (-0.91 m). The data reveals an overall acceleration in coastal retreat, with total system-wide erosion increasing from minimal levels in 2012-2017 to over 5200 m^3 in the most recent period, suggesting intensifying coastal vulnerability.

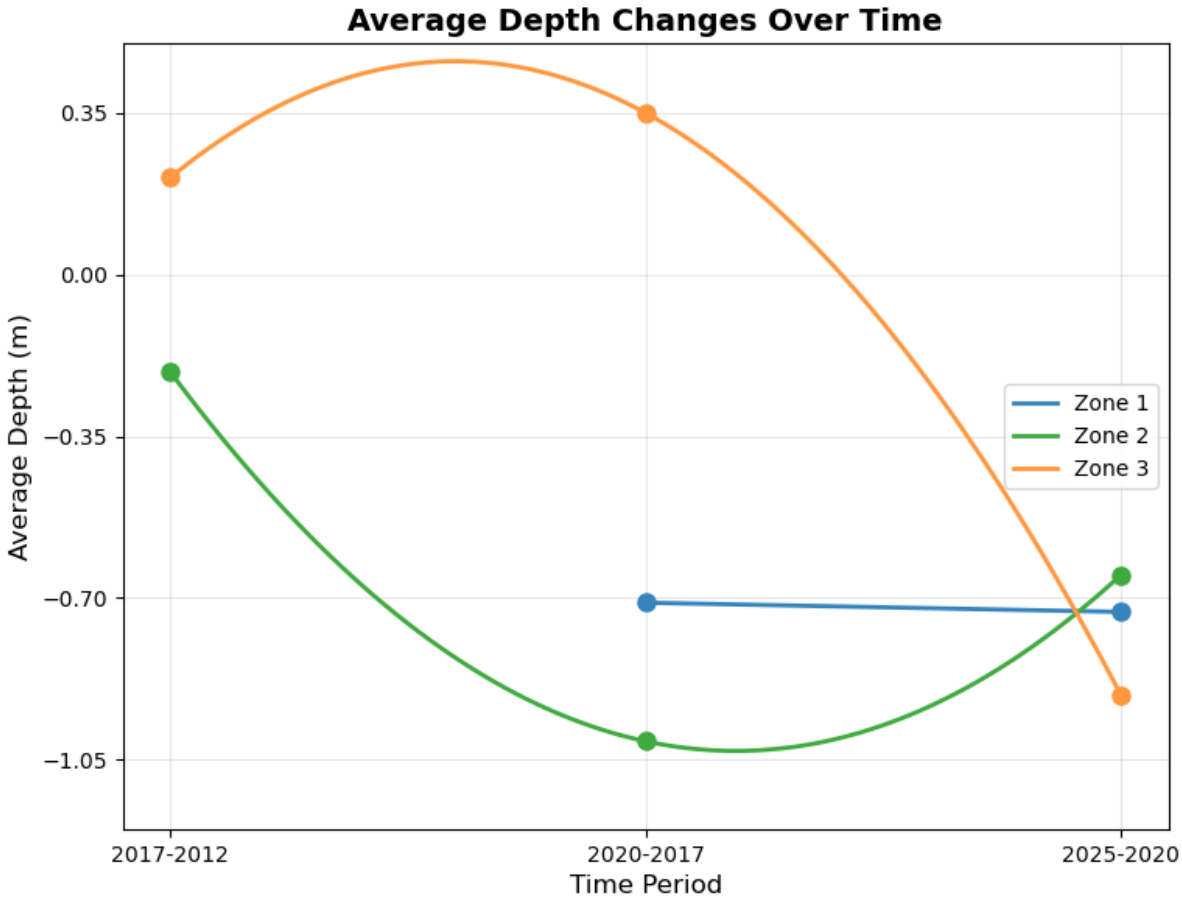

Figure 14 Average depth change

3.3.3 Profile Analysis

A longitudinal profile was extracted from the central portion of all historical shoreline datasets, spanning approximately 600 meters with elevation measurements at 1-meter intervals across the three zones. The longitudinal profile analysis reveals distinct morphological evolution patterns across the study period (Figure 15). Across the entire profile, there is a clear trend of progressive dune elevation lowering over time. The 2012 DTM shows the highest elevations in Zones 2 and 3 where crest heights exceed 5.0 m except the easternmost part where the dune has been accreting from 2012 to 2020. By contrast, the 2025 profile exhibits widespread flat, with average elevations reduced to around 3.3-3.5 m. In Zone 1 (x-axis 0-270 m) the profile drops by over 1 m between 2017 and 2025. In Zone 2 (270-400 m), sharp losses are evident

between 2012 and 2017, 2020 and 2025, during both time periods the dune heights fall by around 1 m. This suggests accelerating erosion in the area adjacent to the golf course fairways. Zone 3 (400-600 m) starts with accretion patterns from 2012 to 2020, but by 2025 also exhibits a downward shift.

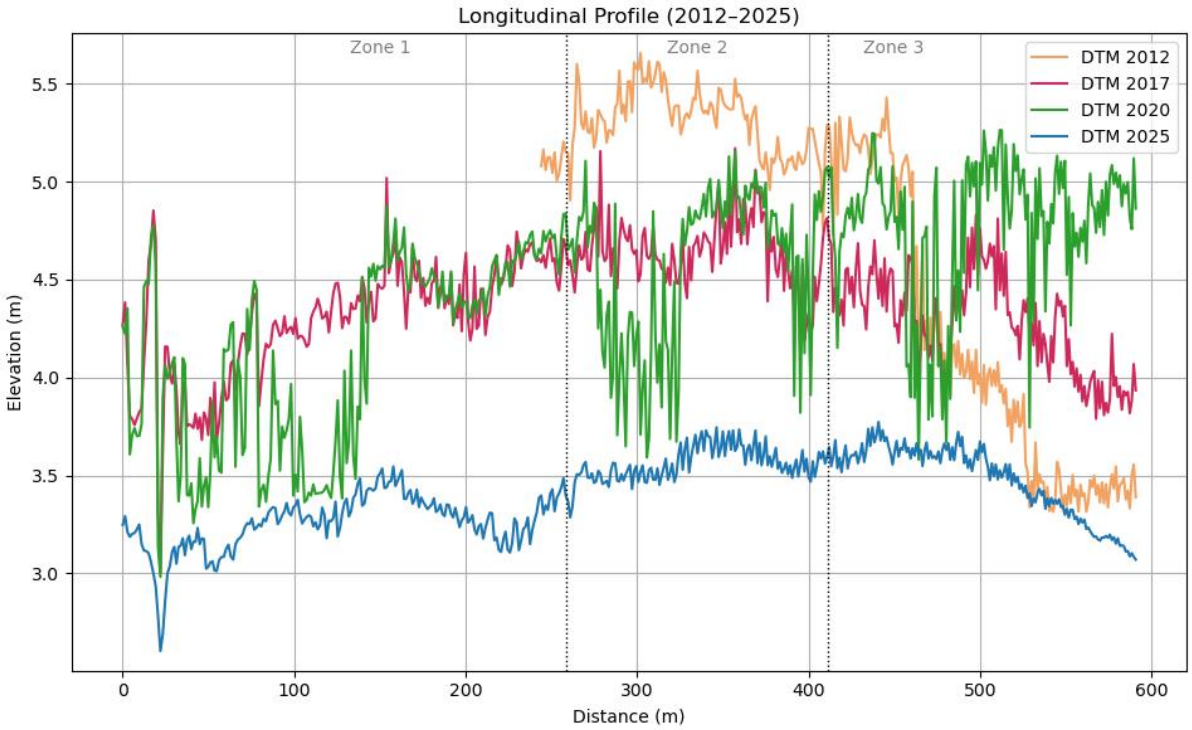

Figure 15 Longitudinal Profile

Cross sectional profiles extracted perpendicular to the shoreline at representative locations within each zone provide detailed insights into the morphological changes observed in the longitudinal analysis (Figure 16-18). The Zone 1 cross section demonstrates pronounced erosional retreat consistent with the longitudinal profile findings of over 1 m elevation loss between 2017 and 2025. The seaward face shows systematic landward migration, with crest elevations declining from 6 m in 2017 to 4 m by 2025, indicating erosion process have completely reshaped the frontal dune morphology. Zone 2 reveals a two-phase erosional pattern: initial crest lowering (2012-2017) followed by wholesale dune removal (2020-2025), supporting the accelerated erosion findings adjacent to the golf course fairways. Zone 3 confirms the accretion to erosion transition identified longitudinally. Crest elevations show an increasing pattern from 2012 to 2020, indicating continued sediment accumulation in the easternmost section. However, by 2025, maximum elevations drop dramatically, marking a fundamental shift from accretional to erosional behaviour.

The cross section analysis reinforces the longitudinal findings of progressive dune degradation while revealing spatial heterogeneity in erosional processes. The progressive decline in elevation across all zones indicates long-term sediment loss and dune degradation, supporting the volumetric analysis findings of accelerated erosion rates.

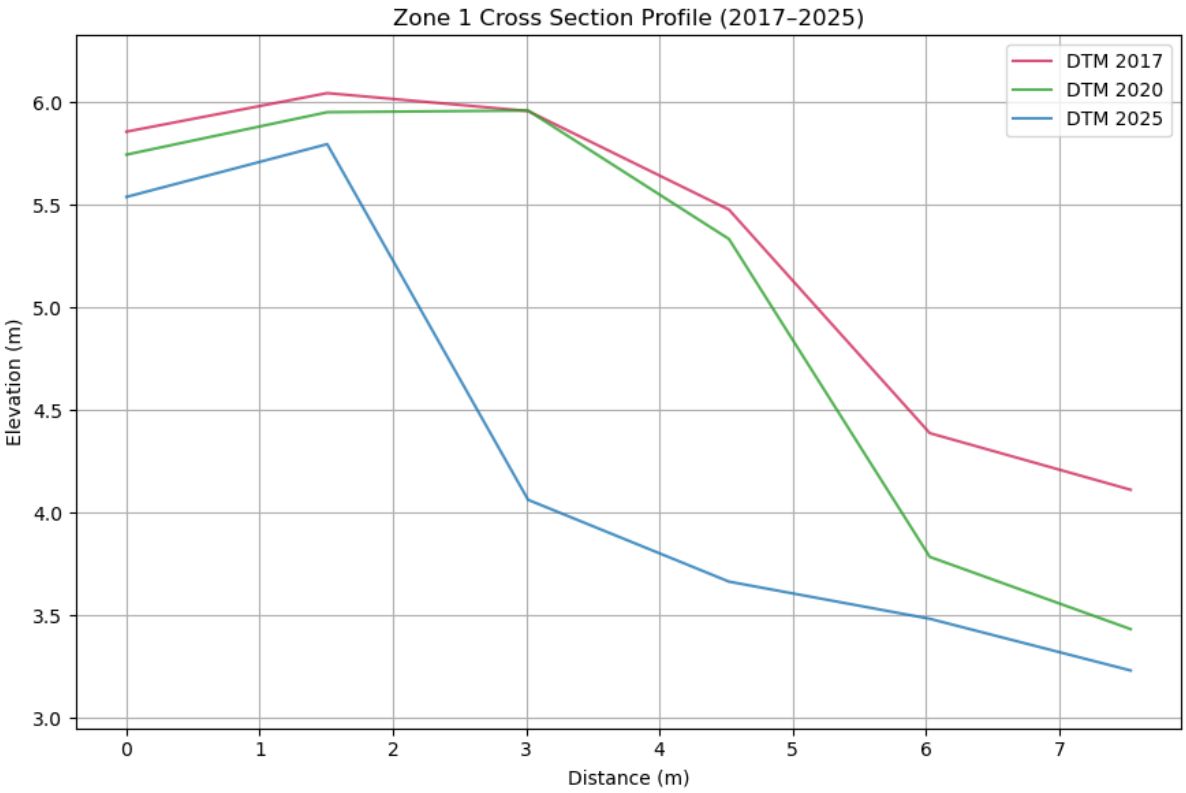

Figure 16 Zone 1 Cross section profile

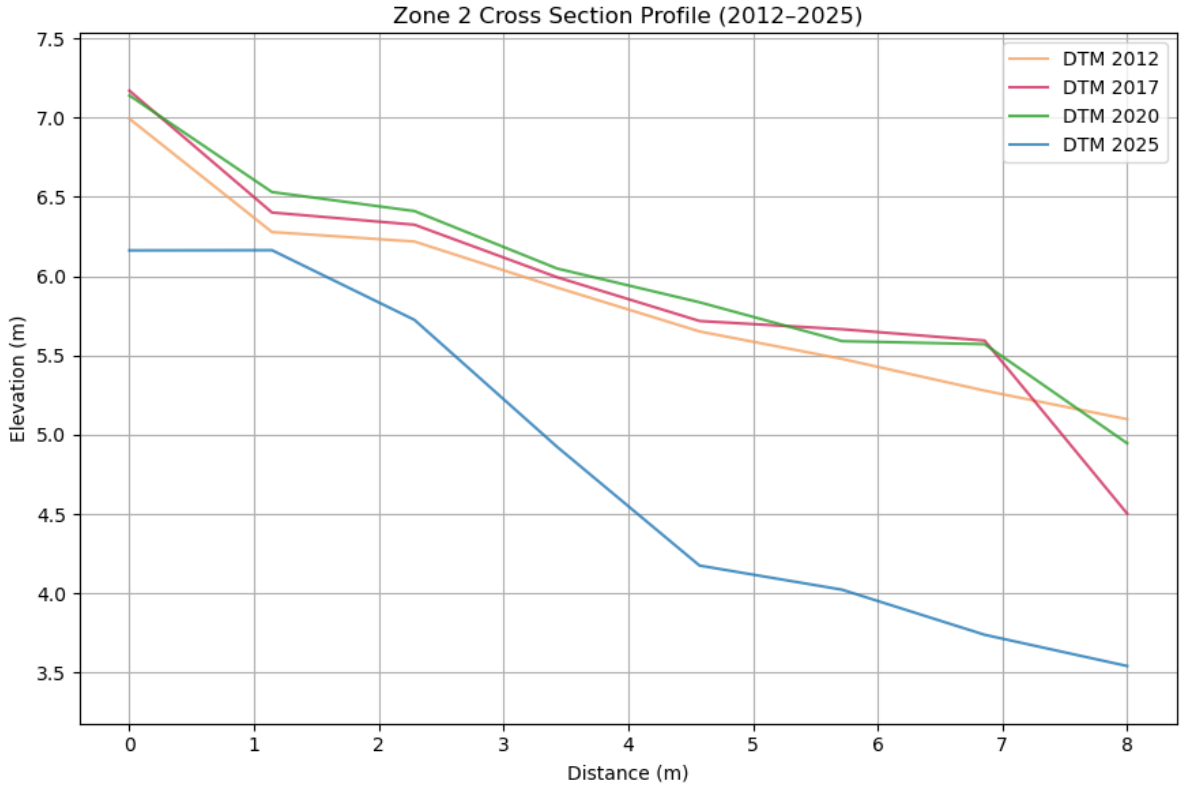

Figure 17 Zone 2 Cross section profile

Figure 18 Zone 3 Cross section profile

4. Discussion

This study set out to assess recent morphological changes in a small coastal dune system in Scotland by integrating UAV-based LiDAR and SfM photogrammetry. Through comparison of two datasets, the research aimed to evaluate the relative accuracy and mapping capabilities of each method for complex, small-scale dune terrain. High resolution terrain models were generated to quantify volumetric change between 2012 and 2025, while spatial analyses identified key zones of erosion. The findings provide a data-driven basis for understanding localised dune dynamics and support recommendations for more adaptive coastal dune monitoring approach.

4.1 Datasets comparison

The comparative analysis between L1 LiDAR and P1 SfM photogrammetry datasets provides valuable insight into sensor performance and the suitability of different monitoring technologies for dune environments. C2C distance comparisons and rasterised DSM differences indicate a high degree of geometric consistency between the two datasets, with most discrepancies falling within ±0.20 m. While localised differences were observed, the overall agreement, indicated by a near-zero mean vertical difference (-0.003 m), confirms that SfM photogrammetry offers sufficient accuracy for detecting meaningful coastal changes. The systematic differences observed between the two datasets in specific terrain types are consistent with the known limitations and strengths of each technology. UAV SfM photogrammetry provides high accuracy mapping of textured anthropic surfaces, while LiDAR excels in penetrating vegetation rich areas (Pinton et al., 2023). In the context of coastal dune monitoring, this translates to SfM photogrammetry performing well on exposed sandy surfaces while showing limitations in vegetated areas where LiDAR maintains superior ground surface detection capabilities (Sestras et al., 2025; Lin et al., 2019; Gonçalves and Henriques, 2015). These findings highlight the practical value of UAV SfM photogrammetry as a reliable and cost-effective tool for dune monitoring. While LiDAR offers better ground-penetrating capability, it requires more complex and expensive configuration. SfM photogrammetry can achieve high resolution surveys with less cost and opens opportunities for more frequent monitoring surveys to capture seasonal dune changes (Gonçalves and Henriques, 2015). The accessibility implications of photogrammetric approaches are particularly significant for coastal management applications (Caroti et al., 2018). Moreover, the accessibility of photogrammetric workflows makes this approach viable for local stakeholders, environmental managers and researchers operating with limited budgets. Open source processing software like QGIS, CloudCompare can support the data processing needs.

4.2 Change Pattern Results Interpretation

4.2.1 Temporal evolution

The results of this study demonstrate patterns of coastal change within the Lundin Links dune system over a 13-year period. Through sequential DoD, volumetric and profile analysis, a

progression from localised sediment accretion to widespread erosion was identified. The transition from initial stability to system wide erosion suggests that the natural buffering capacity of the dune is overwhelmed. This accelerating trend of coastal retreat, particularly the intensification after 2020, indicates that critical thresholds for natural resilience may have been exceeded, with the system transitioning from a self maintaining state to one requiring active management intervention.

This transition from stability to erosion reflects broader patterns observed in Scottish coastal systems. The Dynamic Coast project has shown that the extent of shoreline that is building seawards (accreting) has fallen by 22% (Rennie et al., 2021). The extent eroding has increased, indicating that the Lundin Links system is experiencing changes consistent with national trends. The observed temporal pattern supports findings from coastal vulnerability studies that demonstrate accelerated rates of coastal erosion, exacerbated by climate change and impacting on a relatively densely populated coast (Fitton et al., 2016).

4.2.2 Spatial patterns

The spatial distribution of erosion highlights the vulnerability of certain parts of the dune system. Zone 1 and 2 are both adjacent to actively used golf course fairways, show escalating losses, raising concerns about the exposure of recreational infrastructure to future coastal hazards. The pattern of accelerating erosion observed in this zone highlights the need for proactive management approaches that anticipate and plan for continued coastal retreat rather than attempting to maintain static shoreline positions. The previously stable, even accreting Zone 3 has shifted to a strongly erosional pattern after 2020, indicating that even relatively undisturbed zones are now being affected by changing environmental conditions. The vulnerability of coastal infrastructure to erosion has been highlighted in national assessments, with 3310 dwellings (a value of £524 m) exposed to erosion (Hansom et al., 2016), and the Coastal Erosion Vulnerability Index (CEVI) identifies 1273 of these are also considered to be highly vulnerable to coastal erosion (Rennie et al., 2021). While the golf course represents recreational rather than residential infrastructure, the pattern of increasing erosion adjacent to developed areas is consistent with broader vulnerability patterns.

The profile analysis shows consistent crest lowering and flattening of the dune morphology over time, most notably between 2020 and 2025. This supports the conclusion that the dune system is undergoing a phase of net sediment loss and morphological degradation. The flattening of dune profiles is particularly significant as it reduces the natural storm surge protection capacity of the system, potentially increasing vulnerability to future extreme events (van Wiechen et al. 2023; Fernández-Montblanc et al., 2020, Gorski et al., 2025).

4.2.3 Climate Change and Extreme Event Impacts

The severity and spatial extent of erosion in the most recent period suggest that short term extreme events have played a major role. Storm events like Babet (October 2023) and Éowyn (January 2025) likely caused sudden, severe erosion in the dune system. These events came on top of existing problems like rising sea levels and changing climate. According to the Dynamic Coast project, erosion now affects 46% of Scotland's soft coast, up from 38% in 2017. And the

average shoreline moving inland by about 0.43 meters per year. By 2100, up to 84% of soft coastlines could be eroding if emissions stay high (Dunkley et al., 2021; Rennie et al., 2021). Scotland is also experiencing more extreme weather. The Fife coastline, like much of Scotland's coast, is highly exposed to North Atlantic storm systems and experiences significant wave energy during winter months (Wolf et al., 2020). These storms tend to cause short bursts of damage rather than gradual erosion, making it harder for dunes to recover. Together, these pressures seem to be pushing the Lundin Links dune system beyond its natural resilience threshold. These storms tend to cause short bursts of damage rather than gradual erosion, making it harder for dunes to recover. Together, these pressures seem to be pushing the Lundin Links dune system beyond its natural resilience threshold.

4.3 Limitations and Future Scopes

While this study provides valuable insights into coastal dune change patterns and monitoring methodologies, several limitations should be acknowledged. The focus on a single site limits the generalisability of the findings, and the relatively short time series may not capture longer term cyclical patterns in coastal behaviour. Future research could benefit from expanding the spatial coverage to include multiple dune systems along the Fife coast and extending the temporal analysis to incorporate longer term datasets where available. The integration of additional environmental variables, such as detailed wave climate data, sediment supply assessments, and vegetation change analysis, could provide more comprehensive understanding of the drivers of coastal change. The demonstrated effectiveness of UAV-based monitoring approaches suggests potential for more frequent and flexible assessments of coastal change. This approach is well-suited for routine monitoring or targeted surveys during and after extreme weather events, supporting timely analysis and adaptive coastal management.

5. Conclusion

This study demonstrates the value of integrating UAV LiDAR and UAV SfM photogrammetry to monitor coastal dune dynamics and quantify geomorphic change over time. A detailed comparison showed that both datasets provide high quality topographic data suitable for coastal change analysis. Importantly, the photogrammetric data showed high geometric consistency with LiDAR. The validated UAV SfM photogrammetry method provides stakeholders with a proven tool for ongoing dune monitoring, enabling cost-effective surveillance of vulnerable dune systems protecting coastal infrastructure.

Analysis of multitemporal DEMs revealed a clear progression from localised stability to systemwide erosional retreat, suggesting that recent storm events and cumulative climate stressors may have pushed the system beyond a resilience threshold, threatening the adjacent golf course. The findings align with broader trends of increasing coastal vulnerability in Scotland, as documented in national assessments, underscores the urgency of developing adaptive coastal management strategies that account for dynamic sedimentary systems.

References

Arun, K.S., Huang, T.S. and Blostein, S.D., 1987. Least-Squares Fitting of Two 3-D Point Sets. *IEEE Transactions on Pattern Analysis and Machine Intelligence*, 9(5), pp.698–700. Available at: https://doi.org/10.1109/TPAMI.1987.4767965.

Bakker, J.P. *et al.*, 2016. Environmental Impacts—Coastal Ecosystems. In: M. Quante and F. Colijn, eds. *North Sea Region Climate Change Assessment*. Cham: Springer International Publishing, pp.275–314. Available at: https://doi.org/10.1007/978-3-319-39745-0_9.

Besl, P.J. and McKay, N.D., 1992. A method for registration of 3-D shapes. *IEEE Transactions on Pattern Analysis and Machine Intelligence*, 14(2), pp.239–256. Available at: https://doi.org/10.1109/34.121791.

Caroti, G., Piemonte, A. and Pieracci, Y., 2018. Low-Altitude UAV-Borne Remote Sensing in Dunes Environment: Shoreline Monitoring and Coastal Resilience. In: O. Gervasi *et al.*, eds. *Computational Science and Its Applications – ICCSA 2018*. Cham: Springer International Publishing, pp.281–293. Available at: https://doi.org/10.1007/978-3-319-95174-4_23.

Casella, E. *et al.*, 2020. Accuracy of sand beach topography surveying by drones and photogrammetry. *Geo-Marine Letters*, 40(2), pp.255–268. Available at: https://doi.org/10.1007/s00367-020-00638-8.

Clark, A., Moorman, B.J. and Whalen, D., 2023. UAV-SfM and Geographic Object-Based Image Analysis for Measuring Multi-Temporal Planimetric and Volumetric Erosion of Arctic Coasts. *Canadian Journal of Remote Sensing*, 49(1), p.2211679. Available at: https://doi.org/10.1080/07038992.2023.2211679.

Comba, L. *et al.*, 2018. Unsupervised detection of vineyards by 3D point-cloud UAV photogrammetry for precision agriculture. *Computers and Electronics in Agriculture*, 155, pp.84–95. Available at: https://doi.org/10.1016/j.compag.2018.10.005.

DiGiacomo, A.E. *et al.*, 2020. Modeling Salt Marsh Vegetation Height Using Unoccupied Aircraft Systems and Structure from Motion. *Remote Sensing*, 12(14), p.2333. Available at: https://doi.org/10.3390/rs12142333.

Donker, J., Van Maarseveen, M. and Ruessink, G., 2018. Spatio-Temporal Variations in Foredune Dynamics Determined with Mobile Laser Scanning. *Journal of Marine Science and Engineering*, 6(4), p.126. Available at: https://doi.org/10.3390/jmse6040126.

Dunkley, R.A. *et al.*, 2021. *Dynamic Coast: Mapping Coastal Erosion Disadvantage in Scotland*. Centre of Expertise for Waters. Available at: https://www.dynamiccoast.com/outputs [Accessed 4 Aug. 2025].

Farrell, E.J. *et al.*, 2024. Contemporary research in coastal dunes and aeolian processes. *Earth Surface Processes and Landforms*, 49(1), pp.108–116. Available at: https://doi.org/10.1002/esp.5597.

Feagin, R.A. *et al.*, 2023. Does vegetation accelerate coastal dune erosion during extreme events? *Science Advances*, 9(24), p.eadg7135. Available at: https://doi.org/10.1126/sciadv.adg7135.

Fernández-Montblanc, T., Duo, E. and Ciavola, P., 2020. Dune reconstruction and revegetation as a potential measure to decrease coastal erosion and flooding under extreme storm conditions. *Ocean & Coastal Management*, 188, p.105075. Available at: https://doi.org/10.1016/j.ocecoaman.2019.105075.

Fitton, J.M., Hansom, J.D. and Rennie, A.F., 2016. A national coastal erosion susceptibility model for Scotland. *Ocean & Coastal Management*, 132, pp.80–89. Available at: https://doi.org/10.1016/j.ocecoaman.2016.08.018.

Gomez, C., Hayakawa, Y. and Obanawa, H., 2015. A study of Japanese landscapes using structure from motion derived DSMs and DEMs based on historical aerial photographs. *Geomorphology*, 242, pp.11–20. Available at: https://doi.org/10.1016/j.geomorph.2015.02.021.

Gonçalves, J.A. and Henriques, R., 2015. UAV photogrammetry for topographic monitoring of coastal areas. *ISPRS Journal of Photogrammetry and Remote Sensing*, 104, pp.101–111. Available at: https://doi.org/10.1016/j.isprsjprs.2015.02.009.

Gorski, J.F. *et al.*, 2025. Deterministic, dynamic model forecasts of storm-driven coastal erosion. *Natural Hazards*, 121, pp.6257–6283. Available at: https://doi.org/10.1007/s11069-024-07012-2.

Grohmann, C.H. *et al.*, 2020. Aeolian dune modelling from airborne LiDAR, terrestrial LiDAR and Structure from Motion-Multi View Stereo. *Computers & Geosciences*, 143, p.104569. Available at: https://doi.org/10.1016/j.cageo.2020.104569.

Grottoli, E. *et al.*, 2021. Structure-from-Motion-Derived Digital Surface Models from Historical Aerial Photographs: A New 3D Application for Coastal Dune Monitoring. *Remote Sensing*, 13(1), p.95. Available at: https://doi.org/10.3390/rs13010095.

Hanley, M.E. *et al.*, 2014. Shifting sands? Coastal protection by sand banks, beaches and dunes. *Coastal Engineering*, 87, pp.136–146. Available at: https://doi.org/10.1016/j.coastaleng.2013.10.020.

Hartley, R.J.L. *et al.*, 2020. An Assessment of High-Density UAV Point Clouds for the Measurement of Young Forestry Trials. *Remote Sensing*, 12(24), p.4039. Available at: https://doi.org/10.3390/rs12244039.

Laporte-Fauret, Q. *et al.*, 2019. Low-Cost UAV for High-Resolution and Large-Scale Coastal Dune Change Monitoring Using Photogrammetry. *Journal of Marine Science and Engineering*, 7(3), p.63. Available at: https://doi.org/10.3390/jmse7030063.

Le Mauff, B. *et al.*, 2018. Coastal monitoring solutions of the geomorphological response of beach-dune systems using multi-temporal LiDAR datasets (Vendée coast, France). *Geomorphology*, 304, pp.121–140. Available at: https://doi.org/10.1016/j.geomorph.2017.12.037.

Lin, Y.-C. *et al.*, 2019. Evaluation of UAV LiDAR for Mapping Coastal Environments. *Remote Sensing*, 11(24). Available at: https://doi.org/10.3390/rs11242893.

Mancini, F. *et al.*, 2013. Using Unmanned Aerial Vehicles (UAV) for High-Resolution Reconstruction of Topography: The Structure from Motion Approach on Coastal Environments. *Remote Sensing*, 5(12), pp.6880–6898. Available at: https://doi.org/10.3390/rs5126880.

rapidlasso GmbH, n.d. Overview of all LAStools. Available at: https://rapidlasso.de/product-overview/ [Accessed 4 Aug. 2025].

Pang, T. *et al.*, 2023. Coastal erosion and climate change: A review on coastal-change process and modeling. *Ambio*, 52(12), pp.2034–2052. Available at: https://doi.org/10.1007/s13280-023-01901-9.

Perko, R. *et al.*, 2014. Assessment of the mapping potential of Pléiades stereo and triplet data. *ISPRS Annals of the Photogrammetry, Remote Sensing and Spatial Information Sciences*, II-3, pp.103–109. Available at: https://doi.org/10.5194/isprsannals-II-3-103-2014.

Pinton, D. *et al.*, 2023. Estimating Ground Elevation in Coastal Dunes from High-Resolution UAV-LIDAR Point Clouds and Photogrammetry. *Remote Sensing*, 15(1), p.226. Available at: https://doi.org/10.3390/rs15010226.

Pinton, D., Canestrelli, A. and Fantuzzi, L., 2020. A UAV-Based Dye-Tracking Technique to Measure Surface Velocities over Tidal Channels and Salt Marshes. *Journal of Marine Science and Engineering*, 8(5), p.364. Available at: https://doi.org/10.3390/jmse8050364.

Rebanal Martínez, G., 2021. Golf in St Andrews, the critical years, c. 1880–1914. *Sport in History*, 41(4), pp.524–550. Available at: https://doi.org/10.1080/17460263.2021.1924848.

Rennie, A.F. *et al.*, n.d. *Dynamic Coast Research Summary (2021)*.

Sestras, P. *et al.*, 2025. Land surveying with UAV photogrammetry and LiDAR for optimal building planning. *Automation in Construction*, 173, p.106092. Available at: https://doi.org/10.1016/j.autcon.2025.106092.

Silva, R. *et al.*, 2020. A Framework to Manage Coastal Squeeze. *Sustainability*, 12(24), p.10610. Available at: https://doi.org/10.3390/su122410610.

Skillen, F., Fleming, H. and Beatty, L., 2023. Creating a home for the lived experiences of women club golfers in Scotland: two case studies undertaken in collaboration with the R&A World Golf Museum. *Sport in History*, 43(3), pp.307–331. Available at: https://doi.org/10.1080/17460263.2023.2169747.

Wang, J. *et al.*, 2017. Mapping *Spartina alterniflora* biomass using LiDAR and hyperspectral data. *Remote Sensing*, 9(6). Available at: https://doi.org/10.3390/rs9060589.

Westoby, M.J. *et al.*, 2012. "Structure-from-Motion" photogrammetry: A low-cost, effective tool for geoscience applications. *Geomorphology*, 179, pp.300–314. Available at: https://doi.org/10.1016/j.geomorph.2012.08.021.

van Wiechen, P.P.J. *et al.*, 2023. Dune erosion during storm surges: A review of the observations, physics and modelling of the collision regime. *Coastal Engineering*, 186, p.104383. Available at: https://doi.org/10.1016/j.coastaleng.2023.104383.

Winter, R.C. de and Ruessink, B.G., 2017. Sensitivity analysis of climate change impacts on dune erosion: case study for the Dutch Holland coast. *Climatic Change*, 141(4), pp.685–701. Available at: https://doi.org/10.1007/s10584-017-1922-3.

Wolf, J. *et al.*, 2020. Impacts of climate change on storms and waves relevant to the coastal and marine environment around the UK. *MCCIP Science Review 2020*, pp.132–157. Available at: https://doi.org/10.14465/2020.arc07.saw.

Investigating coastal dune erosion dynamics across Lundin Links golf course using high-resolution UAV imagery

Part II - Technical Report

Table of Contents

Table of Figures

Table of Tables

Software requirement

The software used in this research are listed below:

Software	**Version**	**Task**
Emlid Studio	1.9	Processing ground control points
Pix4DMapper	4.6.4	Photogrammetry processing
CloudCompare	2.12.0	Point cloud processing and comparison
ArcGIS Pro	3.3.1	Map visualisation, raster calculating
QGIS	3.34	Profile lines extracting
LAStools	181001	Generating DEM from point clouds
Visual Studio (Python)	1.92.2	Figure and graph visualisation

1. Introduction

This report expands the details of the research paper “Investigating coastal dune erosion dynamics across Lundin Links golf course using high-resolution UAV imagery” in Part I. It contains the process of data acquisition, general methodology and results processing. This report is divided into the following sections: 2. Data collection, 3. Data processing, 4. Results visualisation, References and Appendices.

2. Data collection

2.1 Public data acquisition

This research acquired historical maps, photogrammetry and LiDAR data through public sources. The historical images are Ordnance Survey maps of National Grid 1:1250 1st Edition (1943-1993), County Series 1:2500 2nd Revision (1906-1939) and aerial images in 2011, 2015, 2020 and 2023 from Digimap (Digimap). These datasets were used for extracting shorelines manually. LiDAR dataset is Scotland Phase 2 (2012), 4 (2017) & 5 (2020) LAS point cloud files at 4 points per metre, 50cm Digital Terrain Model, accessed through the Scottish Remote Sensing Portal (*Scottish LiDAR Remote Sensing datasets | Scottish Government*). These public datasets serve as a foundation for better understanding temporal landscape changes.

2.2 UAV data acquisition

2.2.1 Ground control points

10 GCPs were set up in total across the study area. The number and spatial distribution of GCPs were chosen based on the extent of the survey corridor. The GCPs were surveyed using Emlid RS2+ RTK GNSS receivers operating in real-time kinematic (RTK) mode. The base receiver (designated ARI Emlid RS2+-A) was positioned over GCP26, located at the 4th Tee White marker. The rover unit (DRTK2-A-Ceres) was used to survey the remaining GCPs, beginning at GCP19, located at the 4th Tee Yellow marker. All points were recorded using the Emlid Flow app, taking 3 measurements for each point carefully.

Figure 1 Ground control point and GNSS base station

2.2.2 UAV platform and sensors

In this study, the DJI Matrice 300 RTK platform was selected due to its reliability, robust RTK

positioning capability, and compatibility with advanced aerial sensors. It supports centimetre-level absolute positioning accuracy through its integrated RTK GNSS system, essential for accurate photogrammetric reconstruction and LiDAR data georeferencing. The drone was equipped with two interchangeable sensors:
DJI Zenmuse L1: A LiDAR and RGB camera module, used to capture dense point cloud data with integrated real-time colourisation.
DJI Zenmuse P1: A full-frame photogrammetric RGB camera with a 35 mm and 50 mm lens used for high-resolution imaging and 3D surface modelling.
Table 1 summarizes the planned flight characteristics for both sensors, including nominal survey altitudes, speed, and expected ground sampling distance (GSD).

Table 1 Flight Characteristics

Parameter	L1 LiDAR Survey	P1 Photogrammetry Survey
Sensor	DJI Zenmuse L1	DJI Zenmuse P1
Imagery	LiDAR + RGB	RGB
Survey Height	57 meters AGL	57 meters AGL (35mm) / ~50m (50mm)
Ground Sample Distance	1.56 cm (RGB) / ~997 pts/m² (LiDAR)	0.72 cm (35mm) / est. <1 cm (50mm)
Flight Speed	~5 m/s	~5 m/s

2.2.3 Flight surveys

Data collection was conducted on 1 May 2025 under suitable weather conditions, with wind speeds ranging from 3 to 7.5 m/s, bright but not too strong sunlight, good visibility, and a temperature of approximately 23°C. Safety assessments were conducted before the first flight. The 3 flights were planned and manually operated by Tom Wade. Flights followed a linear corridor aligned with the coastal dune system, extending approximately 10 m inland and 20 m seaward from the dune crest, covering around 580 meters in length.

Figure 2 DJI M300 preparation and taking off

The first flight was launched at 13:56, had a flight duration of 13 minutes, being recovered at 14:09. This flight used the Zenmuse L1 sensor to collect LiDAR data and RGB imagery at an altitude of 57 m AGL and a speed of ~5 m/s. The chosen altitude aligns with Civil Aviation Authority guidelines and ensures safe separation from obstacles within the golf course. LiDAR was captured in single-return mode at 240 kHz, achieving a point density of ~997 pts/m². RGB imagery was acquired simultaneously (GSD: 1.56 cm), with a shutter speed of 1/1000s and auto ISO. The second flight was launched at 14:19, with a 12 minute duration and recovered at 14:31. This flight used the Zenmuse P1 with a 35 mm lens to collect high resolution photogrammetry at the same altitude and speed. Imagery was captured at 1-second intervals with 70/80% side/endlap, achieving a GSD of ~0.72 cm. Oblique surveys (~45°) were completed manually along dune front for both flights to improve 3D surface reconstruction. The third flight was launched at 15:10, had a duration of 9 minutes and being recovered at 15:19. This was conducted manually using the P1 with a 50 mm lens to image a golf hole feature. However, datasets from the oblique survey and the third flight were not used in the study.

3 Data processing

3.1 Georeferencing and Preprocessing in Emlid Studio

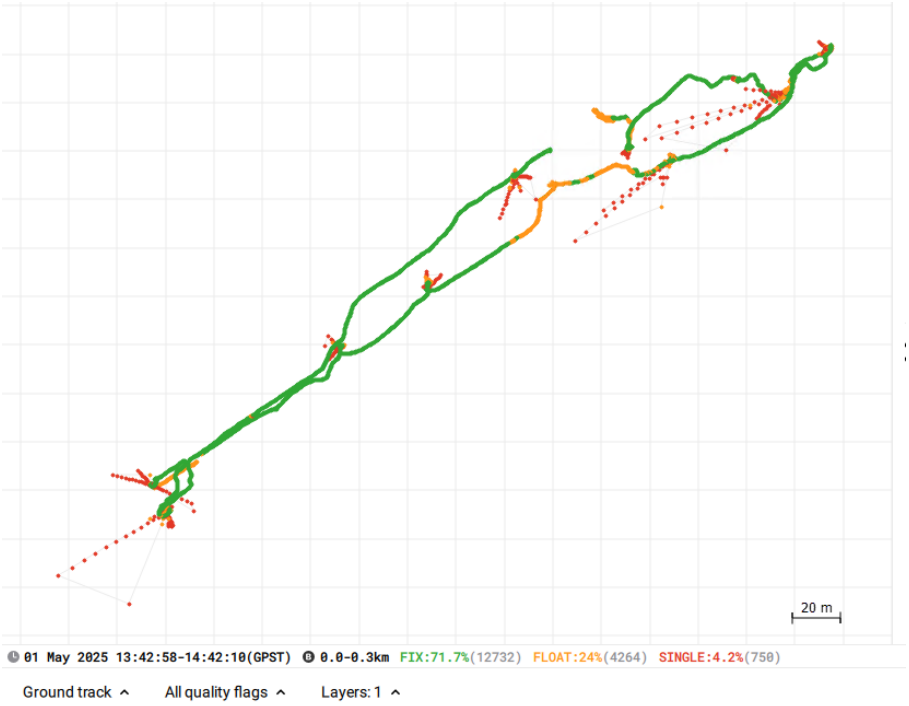

Figure 3 Stop & Go processing in Emlid Studio

Accurate georeferencing and preprocessing was carried out using GNSS data collected with Emlid Reach RS2 units in Emlid Studio (Emlid, 2024) using RINEX data from the OS-Net Dundee (DUDE) CORS station. The workflow included Static processing and Stop-and-Go Processing. In Static processing, the base station (located at GCP 19) coordinates (in WGS-84 with ellipsoidal height) were corrected using PPK (Post-Processed Kinematic) methods. In Stop-and-Go Processing, GCPs were processed relative to the corrected base. The resulting positions were averaged manually in Microsoft Excel. The corrected base station coordinates were used in DJI Terra (processed by Tom Wade) to georeference the LiDAR data and export it in standard .LAS format. Corrected GCPs were imported into Pix4D (Pix4D, 2021) to support accurate initial alignment and georeferencing for photogrammetry.

Both photogrammetry and LiDAR datasets included nadir and oblique acquisition configurations. The nadir-only LiDAR dataset was found to be cleaner with less noise and provided adequate point density on the dune front. To ensure methodological consistency, nadir-only datasets were selected for both sensors.

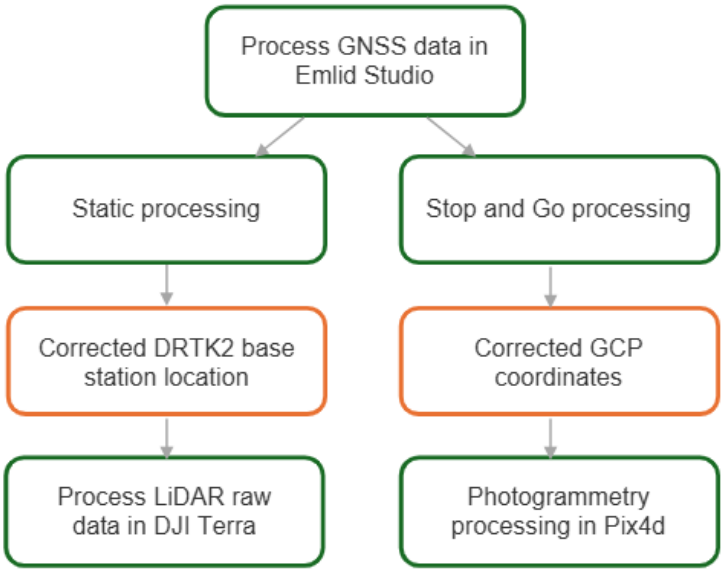

Figure 4 Georeferencing and Preprocessing Workflow

3.2 Photogrammetric processing in Pix4DMapper

Once the GCPs were processed and georeferenced, the photogrammetric processing was performed using Pix4D. After importing the image dataset into Pix4D, Step 1: Initial Processing started. Pix4D automatically carried out the image alignment, creating a sparse point cloud from the images. The software used the marked GCPs to adjust the camera positions and orientations, improving the georeferencing accuracy. In Step 2: Point Cloud and Mesh, Pix4D used the aligned images to generate a dense point cloud. This process involved matching features across multiple images to improve the accuracy of the 3D mesh. In Step 3 DSM, Orthomosaic and Index, the dense point cloud was used to generate an orthophoto and DSM for visualisation. These products provided high-resolution, accurate representation of the study area, ready for further analysis.

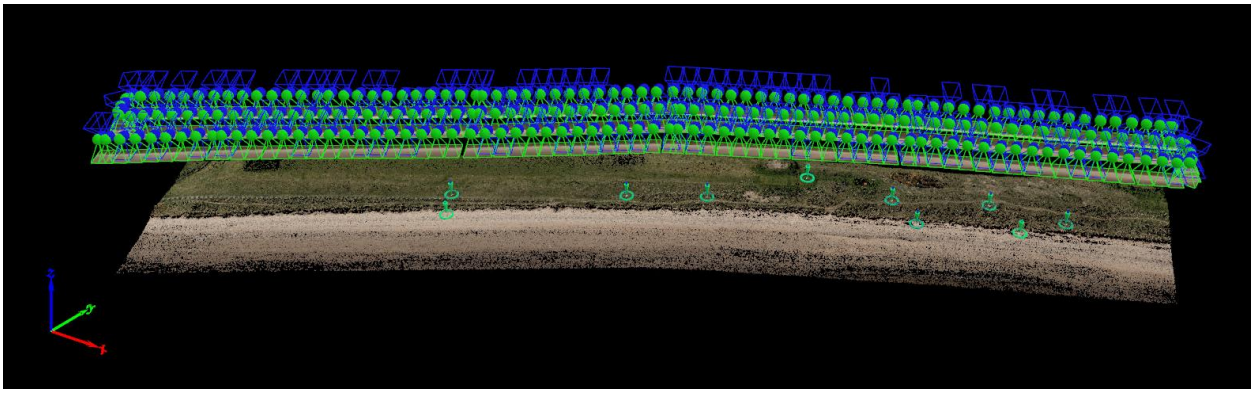

Figure 5 P1 point cloud in Pix4DMapper

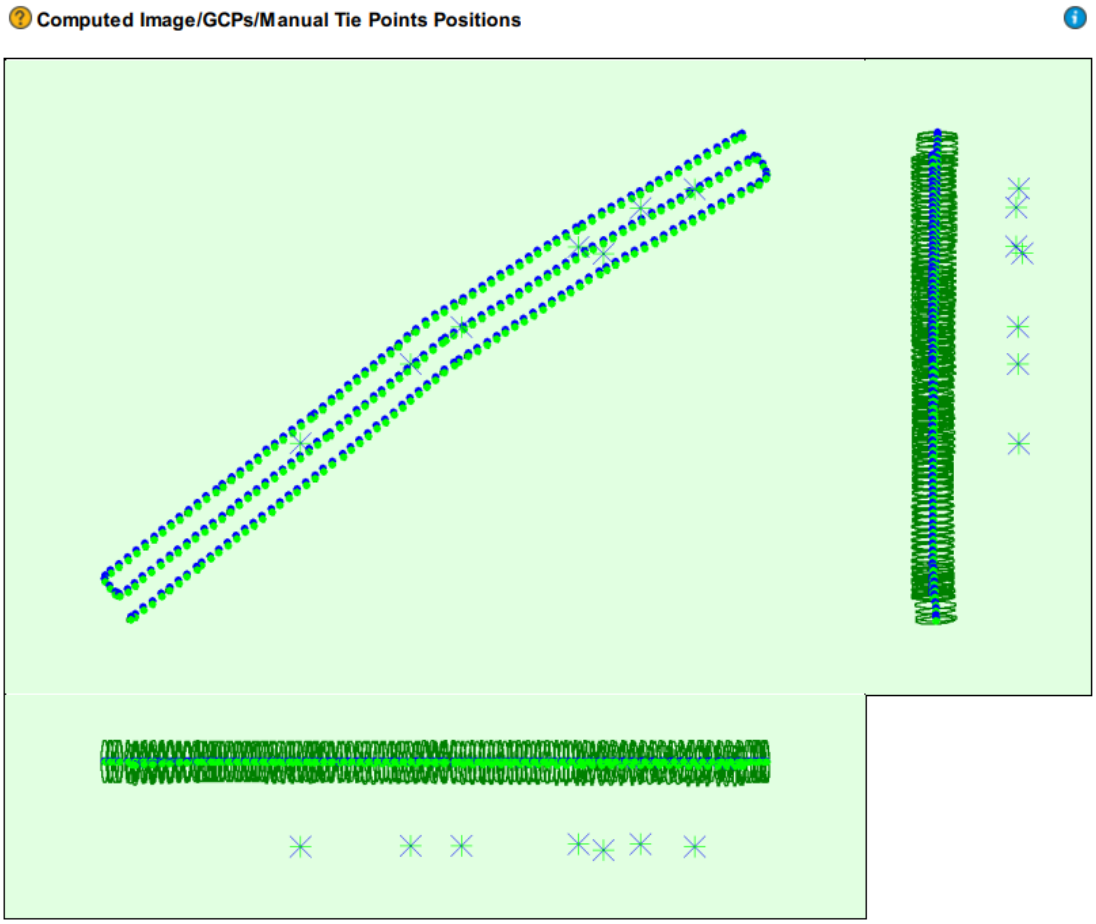

Figure 6 Computed GCP positions from photogrammetric processing quality report

The mean GCP Root Mean Square Error (RMSE) for the seven ground control points used was: X: 0.008 m, Y: 0.012 m, Z: 0.017 m. These sub-decimetre errors reflect strong alignment between the photogrammetric model and the GNSS surveyed GCPs. The mean reprojection error for all GCPs was approximately 0.51 pixels, indicating accurate tie point identification and stable geometry. Three independent check points were also used to assess absolute model accuracy. The mean RMSE for these was: X: 0.012 m, Y: 0.012 m, Z: 0.058 m. These values confirm that vertical errors (Z) are slightly higher, as is common in UAV photogrammetry, particularly over vegetated and steep dune terrain. Nevertheless, the sub-6 cm vertical RMSE is well within the expected error range for UAV-based mapping at this resolution and meets the accuracy requirements for coastal monitoring applications. Detailed GCP and check point error values are provided in Appendix B.

3.3 Point clouds Co-Registration

Due to observed spatial offsets between the LiDAR and photogrammetry derived point cloud in CloudCompare (CloudCompare, 2022), co-registration was performed to ensure consistency before comparing outputs. The LiDAR point cloud was used as the reference dataset for

alignment due to its higher absolute positional accuracy. The Iterative Closest Point (ICP) algorithm was applied in CloudCompare to align two point clouds.

3.4 DTM and DSM generation

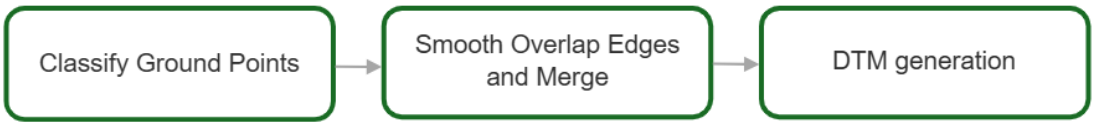

Figure 7 DTM generation using LAStools workflow

Initial trials using Cloth Simulation Filter (CSF) in CloudCompare produced overly aggressive results like partial removal of the coastal dune surface. LAStools (rapidlasso GmbH, 2018) was then selected for generating DTMs for both LiDAR and Photogrammetric data since it offers detailed control over ground classification for high resolution imagery. It allows preserving important micro topography like coastal dunes. This study employed lasground_new tool in LAStools, which implements a Progressive TIN Densification (PTD) algorithm with parameter customisation (e.g., -step, -spike, -bulge, -offset) (rapidlasso GmbH, 2018).

- -step: Defines the spacing of the grid used during ground point estimation. Smaller values help preserve small terrain features.
- -bulge: Controls how aggressively the algorithm treats low vegetation and bumps as ground. Higher values reduce ground misclassification under vegetation.
- -spike: Prevents isolated high points (e.g., shrubs) from being classified as ground by setting a height tolerance.
- -offset: Adjusts the vertical buffer for initial ground estimation, useful for steep or varied terrain.

This method preserved delicate terrain structures and suits better for the high density point clouds. Then lasthin was used to reduce point density while keeping the cleanest point in each 0.25 m cell. It also removed tile edges and overlaps for 4 photogrammetry point clouds before merging, ensuring a seamless DTM grid. The classified, thinned tiles were then merged using lasmerge, retaining only points classified as ground (class 2). Finally, las2dem was used to rasterise the ground point cloud into a 0.25 m resolution DTM (see appendix C for full command).

The DSMs were generated using the Rasterize tool in CloudCompare, with the maximum height option to represent the uppermost surface including vegetation and structures. Using the max value per grid cell ensures that these surface features are retained, which is important for understanding vegetation cover, shadow effects in photogrammetry, and the distinction between DSM and DTM.

4 Results Visualisation

4.1 LiDAR and Photogrammetric data comparison

To assess the performance of the LiDAR and photogrammetric datasets collected in UAV survey, several comparison methods were applied to both point cloud(3D) and raster(2D) levels. The objective was to evaluate spatial differences, identify limitations in data quality, and select the appropriate inputs for further change analysis.

4.1.1 Point cloud comparison (3D)

After the two point clouds are aligned, a comparison was performed using the Cloud-to-Cloud (C2C) distance tool in CloudCompare. The LiDAR point cloud was selected as the reference dataset due to its larger coverage and robustness in capturing ground surfaces, especially in vegetated or steep terrain. The C2C tool computes the Euclidean distance from each point in the photogrammetry cloud to the nearest surface in the LiDAR cloud. The result is a 3D distance map that visually represents spatial mismatches. Figure 8 shows a screenshot of the overlaid point clouds and the corresponding C2C distance output in CloudCompare.

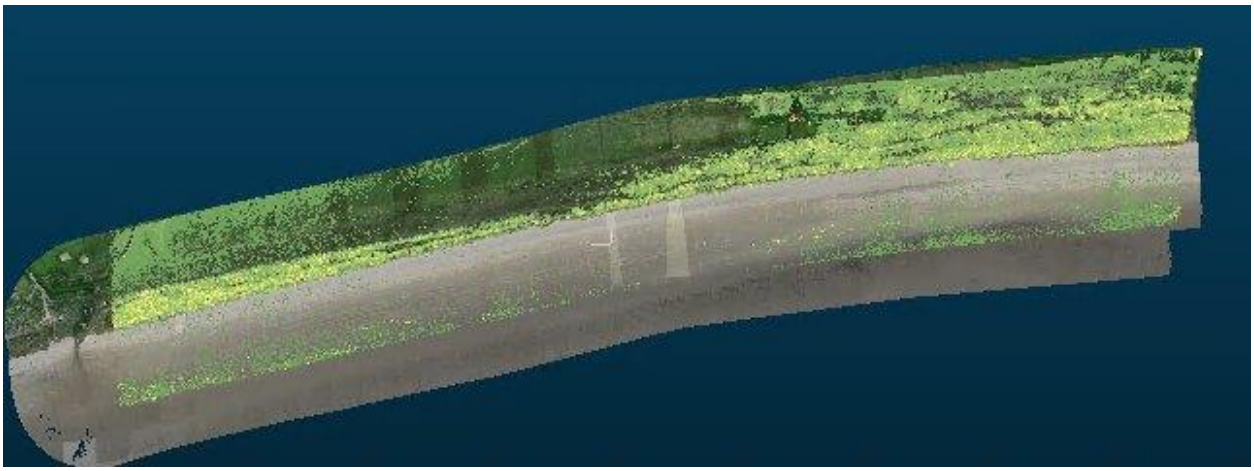

Figure 8 Cloud-to-cloud comparison of LiDAR and photogrammetric point clouds in CloudCompare

The result is a scalar distance value for each point in the compared cloud, representing how far it deviates from the reference. This method does not require any surface reconstruction (e.g., mesh or DEM generation), making it a fast and flexible tool for initial inspection of point cloud alignment or changes over time. However, because it is point-to-point and directionless, C2C is sensitive to point density, noise, and registration quality. It may overestimate distances in sparse or noisy regions (e.g., vegetation) and does not distinguish between vertical and horizontal displacements (CloudCompare, 2022).

4.1.2 Raster-Based DSM Comparison (2D)

To further evaluate the datasets at a raster level, the DSMs generated from both point clouds were differenced using the Raster Calculator to produce a layer representing vertical height differences (P1 DSM − L1 DSM). Unlike the C2C method, this approach captures vertical elevation differences (Z value), reflecting how photogrammetric surface heights deviate from LiDAR-derived surfaces. The resulting DSM of Difference displayed some systematic deviations, particularly in dune areas. Negative values in the output suggest that P1-derived elevations were lower than those from the LiDAR dataset.

A notable pattern observed in the DSM of difference was the presence of negative values in dune crest and slope areas in the photogrammetry dataset.
A zoomed-in dune front comparison (Figure 9) illustrates this issue. It shows that the P1 data had fewer points and less surface definition, contributing to negative elevation differences in the DSM output. Figure 9 shows the point cloud density contrast along the same part of the dune front.

Figure 9 Point cloud of dune front showing lower density and reduced surface capture in the photogrammetry (left) dataset compared with the LiDAR (right) one

4.1.3 DSM Difference Statistics

Statistical analysis was performed on the DSM difference raster to quantify overall vertical discrepancies between the datasets. Table 2 provides a summary of the vertical differences across the study area and helps quantify the level of agreement between the two datasets.

Table 2 Elevation difference statistics between P1 DSM and L1 DSM

Statistics	Min	Max	Mean	Std. Dev.
Value (m)	-2.1331	11.04	-0.0029	0.2029

The mean difference is close to zero (-0.0029 m), indicating the two DSMs align well in elevation overall. However, the presence of extreme minimum (-2.13 m) and maximum (11.04 m) values in the DSM difference, suggesting that outliers exist in localised areas. These are less

likely caused by misalignment, but how the two sensors capture and reconstruct surface features differently.

Negative values are mostly concentrated along the dune front, where P1 data had fewer points. This occurs because steep dune faces create shadows in aerial imagery, resulting in reduced point density and requiring interpolation that smooths the terrain surface. The near-vertical dune front also limits accurate photogrammetric reconstruction from nadir viewing angles. Positive values occur in more vegetated areas where photogrammetry recorded higher elevations than LiDAR. This reflects how the sensors capture vegetation differently, as photogrammetry reconstructs the visible canopy surface, while LiDAR's active laser pulses can penetrate vegetation and represent the filtered ground surface. The standard deviation of 0.20 m reflects the general vertical variation between the two surfaces is low, confirming that significant differences are localised to specific terrain types rather than widespread across the study area.

In summary, the photogrammetry provides adequate accuracy for coastal dune monitoring, with near-zero mean difference and low standard deviation when comparing results with LiDAR derived DSM. From a practical perspective, photogrammetry offers more cost advantage for routine coastal monitoring with lower expenses, high resolution and accessibility compared with LiDAR. However, LiDAR remains justified for applications requiring detailed terrain characterisation. Therefore, for the temporal analysis LiDAR data is utilised to maintain consistency with historical LiDAR datasets from government portals, supporting assessment of long-term coastal change patterns.

4.2 Temporal change analysis

To quantify topographic change across the study site during 2012 to 2025, DEMs of Difference (DoD), volumetric analysis, and topographic profile comparisons were conducted based on L1 DTMs to assess spatial and temporal erosion/accretion patterns.

4.2.1 DEM of difference (DoD)

Input datasets included L1 DTMs from 2012, 2017, 2020, and 2025. DEM differencing was conducted in ArcGIS Pro (Esri, 2024) using the Raster Calculator. For each time interval (2012–2017, 2017–2020, 2020–2025, and 2012–2025), the later DTM was subtracted from the earlier one to produce raster surfaces showing elevation change. Each DoD raster was visualised with a diverging colour ramp (red = gain, blue = loss) to facilitate interpretation of spatial patterns. Annual rate of elevation change was calculated by dividing each DoD raster by the number of years in its respective period. This normalisation enabled comparison across unequal intervals and highlighted areas of consistent morphological change. Rate change map was generated using the Raster Calculator and displayed in units of metres per year (m/yr). All DoD rasters were produced at 0.5 m pixel resolution, consistent with the resolution of the input DTMs derived from historical datasets.

To account for uncertainty and non significant change, a threshold of ±0.3 m was defined as

stable area in each DoD. This threshold covers to the vertical accuracy of the DTM and the propagated error between datasets. All elevation changes smaller than ±5 cm were considered within the noise range and were included in this threshold. This ensures that only statistically meaningful topographic changes were retained for spatial analysis.

Figure 10 Example of DoD map

4.2.2 Volumetric Analysis

Volumetric change was computed from the DoD rasters using "Zonal Statistics" tool in ArcGIS. The dune system was divided into three spatial zones to examine patterns of change alongshore and across the dune width. For each zone and time interval, net elevation change was multiplied by cell area to derive total volume loss or gain.

The calculation process began with DoD generation, where DTM for each survey period were subtracted to create difference rasters showing elevation change between time periods. A minimum level of detection threshold was subsequently applied to filter noise and ensure statistical significance of measured changes. Vector polygons defining each zone boundary were used as analysis masks for the zonal statistics computation. For each zone, positive elevation changes (accretion) and negative changes (erosion) were calculated separately by summing the product of elevation change and pixel area. The spatial extent of erosion and accretion within each zone was quantified by counting affected pixels and converting to square

meters. Table 3 shows the resulting values and were visualised using bar chart (Figure 11).

Table 3 Volume change for each zone and period

time	pattern	zone1	zone2	zone3	sum
2025-2020	erosion volume	-2061.48	-1304.55	-1885.17	-5251.19
	erosion area	2817.798	1993.918	2063.315	6862
	accretion volume	0	0	0	0
	accretion area	0	0	0	0
2020-2017	erosion volume	-2410.73	-2275.09	-705.659	-5391.48
	erosion area	1812.75	1381.75	875	4069.5
	accretion volume	412.6912	258.6285	1429.683	2101.002
	accretion area	999.75	607.5	1175.5	2782.75
2017-2012	erosion volume	no data	-588.438	-180.017	-768.454
	erosion area		1108	355	1463
	accretion volume		172.6474	600.562	773.2094
	accretion area		882	1686	2568

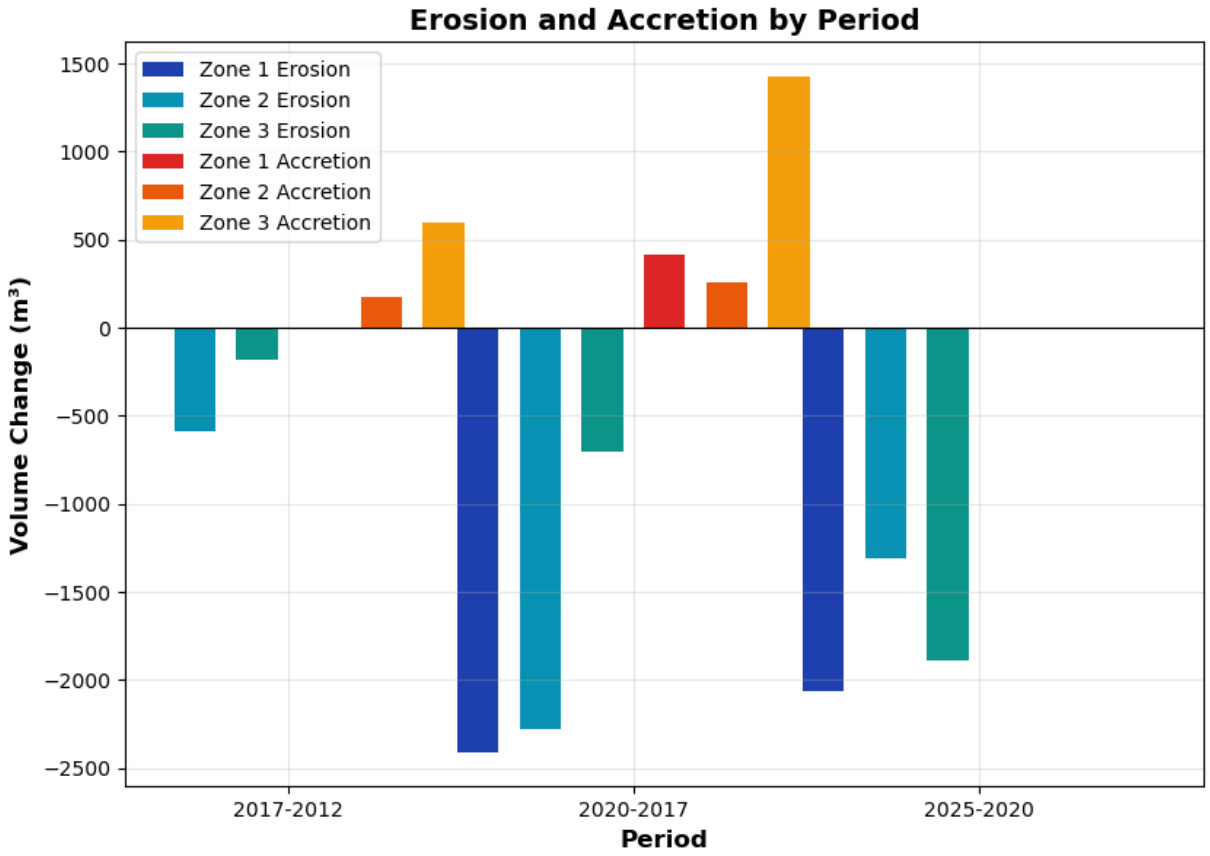

Figure 11 Erosion and Accretion Volume

Average depth change calculations (Table 4) were derived from the volumetric analysis results to provide normalised measures of morphological change intensity across zones of varying size. The calculation methodology involved determining the total area affected by combining both erosional and accretional areas within each zone for each period. Total volume change was computed as the net difference between erosion and accretion volumes, with erosional volumes treated as negative values and accretional volumes as positive values. The net average depth for each zone and period was calculated by dividing the total volume change by the total area affected within that zone. This approach provides a standardised metric that accounts for the spatial extent of change while normalising for zone size differences. Areas affected represent the combined spatial footprint of both erosional and accretional processes within each zone. This method enables direct comparison of morphological change intensity between zones of different sizes and across different time periods. The resulting depth values indicate the average vertical change experienced across the morphologically active portions of each zone, with negative values representing net lowering and positive values indicating net elevation gain.

Table 4 Depth change statistics

Period	Zone	Total Volume Change (m^3)	Area Affected (m^2)	Net Avg Depth (m)
2025-2020	Zone 1	-2,061.48	2,817.80	-0.73
	Zone 2	-1,304.55	1,993.92	-0.65
	Zone 3	-1,885.17	2,063.31	-0.91
2020-2017	Zone 1	-1,998.04	2,812.50	-0.71
	Zone 2	-2,016.46	1,989.25	-1.01
	Zone 3	724.02	2,050.50	0.35
2017-2012	Zone 1	—	—	—
	Zone 2	-415.79	1,990.00	-0.21
	Zone 3	420.54	2,041.00	0.21

4.2.3 Profile Analysis

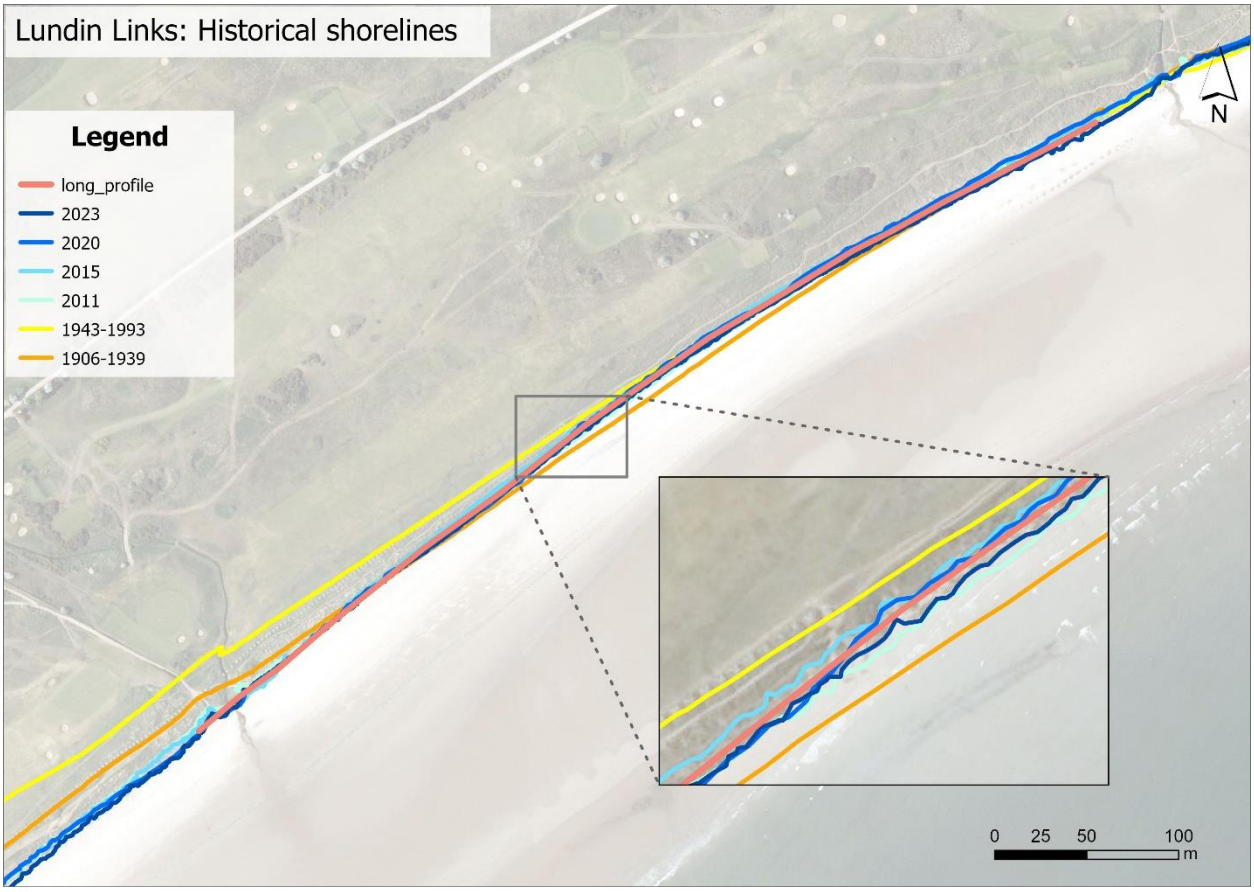

Figure 12 Selected longitudinal line (pink) and historical shorelines

Historical shorelines were extracted from public aerial imagery. A selected longitudinal line was manually drawn by estimating the middle line from them, run parallel to the coastline to assess changes along the crest and foredune alignment. Three cross section lines were also manually selected from 3 zones, which extend perpendicular to the shoreline to visualise slope retreat, elevation loss, and toe migration in three zones. Topographic profiles from all periods were extracted from these lines to analyse detailed morphological changes across the dune system over time.

The profile extraction was conducted Using the Profile Tool in QGIS (QGIS Development Team, 2023), elevation values were sampled from each DoD along the selected transect line, transects were digitised based on the spatial structure of the dune system. These datasets were exported as CSV files and processed in Python (Microsoft, 2025) for further analysis. Profile graphs were then generated to visualise changes in elevation over time. The longitudinal profile was positioned to represent the approximate average of all historical shoreline positions, offering a consistent basis for temporal comparison. Cross-section profiles were distributed across the width of the dune system to capture representative topographic change from the seaward edge to the landward margin.

Reference

CloudCompare (2022) CloudCompare (v. 2.12.0 – “Kyiv”) [Software]. CloudCompare. Available at: https://www.cloudcompare.org (Accessed: 3 August 2025).

DJI Matrice 300 RTK – Support and Downloads [Online]. DJI. Available at: https://www.dji.com/matrice-300/downloads (Accessed: 3 August 2025).

Emlid (2024) Emlid Studio (v. 1.9) [Software]. Emlid. Available at: https://emlid.com/emlid-studio/ (Accessed: 3 August 2025).

Esri (2024) ArcGIS Pro (v. 3.3.1) [Software]. Esri. Available at: https://support.esri.com/en-us/knowledge-base/faq-what-are-the-build-numbers-for-releases-of-arcgis-p-000012500 (Accessed: 3 August 2025).

Microsoft (2025) Python extension for Visual Studio Code (v. 1.92.2) [Software]. Visual Studio Marketplace. Available at: https://marketplace.visualstudio.com/items?itemName=ms-python.python (Accessed: 3 August 2025).

Pix4D (2021) PIX4Dmapper (v. 4.6.4) [Software]. Pix4D. Available at: https://www.pix4d.com/product/pix4dmapper-photogrammetry-software/ (Accessed: 3 August 2025).

QGIS Development Team (2023) QGIS (v. 3.34 “Prizren”) [Software]. QGIS.org. Available at: https://blog.qgis.org/2023/11/05/qgis-3-34-prizren-is-released/ (Accessed: 3 August 2025).

rapidlasso GmbH (2018) LAStools (v. 181001) [Software]. rapidlasso.com. Available at: https://rapidlasso.com/lastools/ (Accessed: 3 August 2025).

Appendices

A: UAV Flight mission record

Sensor Type	Start	End	Parameters	Notes
DJI Zenmuse L1 (LiDAR + RGB)	13:56	14:09	**Flight mode:** Terrain-follow (OS 5 m DEM) **Speed:** 5 m/s **Altitude (AGL):** 57 m **Coverage:** 10 m inland, 20 m seaward of CL **LiDAR density:** 997 pts/m² **LiDAR mode:** Single return, 240 kHz **RGB GSD:** 1.56 cm **RGB overlap:** 60% sidelap / 70% endlap **Camera settings:** Shutter priority, 1/1000 s, auto ISO, EV -0.3	Manual oblique pass added after main survey
DJI Zenmuse P1 (35 mm)	14:19	14:31	**Flight mode:** Terrain-follow (OS 5 m DEM) **Speed:** 5 m/s **Altitude (AGL):** 57 m **Coverage:** Same transect as above **RGB GSD:** 0.72 cm **RGB overlap:** 70% sidelap / 80% endlap **Camera settings:** Manual mode, f/5.6, 1/1000 s, auto ISO	Followed by manual obliques (~45°); landing images excluded
DJI Zenmuse P1 (50 mm)	15:10	15:19	**Flight mode:** Manual **Altitude (AGL):** ~50 m **Capture type:** Orbit + two-axis cross transects **Image type:** Nadir and oblique **Interval:** 1 s **Camera settings:** Manual mode, f/5.6, 1/1000 s, auto ISO	Contextual imaging of golf course terrain

B: Pix4D GCP and Check Point Error

GCP Name	Accuracy XY / Z (m)	Error X (m)	Error Y (m)	Error Z (m)	Projection Error (px)	Verified / Marked

28	0.020 / 0.020	-0.000	-0.016	0.027	0.449	15 / 15
65	0.020 / 0.020	0.006	-0.002	-0.012	0.534	15 / 15
21	0.020 / 0.020	0.007	0.021	0.012	0.491	15 / 15
7	0.020 / 0.020	-0.005	0.002	0.020	0.460	17 / 17
8	0.020 / 0.020	-0.014	-0.016	-0.014	0.634	16 / 16
9	0.020 / 0.020	-0.003	0.005	-0.019	0.559	15 / 15
62	0.020 / 0.020	0.009	0.006	-0.014	0.382	15 / 15
Mean (m)		-0.00003	0.00007	0.00006		
Sigma (m)		0.00754	0.01227	0.01739		
RMS Error (m)		0.00754	0.01228	0.01739		

Check Point Name	Error X (m)	Error Y (m)	Error Z (m)	Projection Error (px)	Verified / Marked
64	-0.0040	0.0053	-0.0581	0.425	17 / 17
15	0.0045	0.0127	-0.0028	0.487	17 / 17
19	-0.0194	-0.0150	0.0809	0.551	10 / 10
Mean (m)	-0.00632	0.00099	0.00666		
Sigma (m)	0.00991	0.01174	0.05713		
RMS Error (m)	0.01176	0.01178	0.05751		

C: LAStools command

1. Classifying the point cloud:
E:\>U:\SCE\GEOS\LAStools\bin\lasground_new.exe -i E:\ARI\K\point_cloud*.las -odir E:\ARI\K\P1class -olas -step 0.5 -spike 0.5 -bulge 0.3 -down_spike 1.0 -thin_with_grid 0.15

2. Smooth overlaps using lasthin before merging:

E:\>U:\SCE\GEOS\LAStools\bin\lasthin.exe -i E:\ARI\K\P1class*.las -step 0.25 -highest -odir E:\ARI\K\thinned -olas

3. Merge 4 las files that pix4d generated:

E:\>U:\SCE\GEOS\LAStools\bin\lasmerge.exe -i E:\ARI\K\thinned*.las -keep_class 2 -o E:\ARI\K\P1ground_thinned.las

4. DTM generating:

E:\>U:\SCE\GEOS\LAStools\bin\las2dem.exe -i E:\ARI\K\P1ground_thinned.las -o E:\ARI\K\dtm_p1.tif -step 0.25 -keep_class 2 -otif

D: Python code

D1 Volumetric Change visualisation

```
import matplotlib.pyplot as plt
import numpy as np
```

```
import pandas as pd

# Data preparation
data = {
    'Period': ['2017-2012', '2020-2017', '2025-2020'],
    'Zone 1 Erosion': [np.nan, -2410.73, -2061.48],
    'Zone 1 Accretion': [np.nan, 412.69, 0],
    'Zone 2 Erosion': [-588.44, -2275.09, -1304.55],
    'Zone 2 Accretion': [172.65, 258.63, 0],
    'Zone 3 Erosion': [-180.02, -705.66, -1885.17],
    'Zone 3 Accretion': [600.56, 1429.68, 0]
}

net_data = {
    'Period': ['2017-2012', '2020-2017', '2025-2020'],
    'Zone 1': [np.nan, -1998.04, -2061.48],
    'Zone 2': [-415.79, -2016.46, -1304.55],
    'Zone 3': [420.54, 724.02, -1885.17]
}

df = pd.DataFrame(data)
net_df = pd.DataFrame(net_data)

# Color schemes
erosion_colors = ['#1e40af', '#0891b2', '#0d9488']
accretion_colors = ['#dc2626','#ea580c', '#f59e0b']
net_colors = ['#1f77b4', '#2ca02c', '#ff7f0e']

def plot_erosion_accretion():
    fig, ax = plt.subplots(figsize=(14, 8))

    x = np.arange(len(df['Period']))
    width = 0.12
    spacing = 0.18  # Larger than width to create gap

    # Erosion bars
    ax.bar(x - 2.5*spacing, df['Zone 1 Erosion'], width,
label='Zone 1 Erosion', color=erosion_colors[0])
    ax.bar(x - 1.5*spacing, df['Zone 2 Erosion'], width,
label='Zone 2 Erosion', color=erosion_colors[1])
    ax.bar(x - 0.5*spacing, df['Zone 3 Erosion'], width,
label='Zone 3 Erosion', color=erosion_colors[2])

    # Accretion bars
    ax.bar(x + 0.5*spacing, df['Zone 1 Accretion'], width,
label='Zone 1 Accretion', color=accretion_colors[0])
    ax.bar(x + 1.5*spacing, df['Zone 2 Accretion'], width,
label='Zone 2 Accretion', color=accretion_colors[1])
```

```
    ax.bar(x + 2.5*spacing, df['Zone 3 Accretion'], width,
label='Zone 3 Accretion', color=accretion_colors[2])

    ax.set_xlabel('Period', fontsize=12, fontweight='bold')
    ax.set_ylabel('Volume Change (m³)', fontsize=12,
fontweight='bold')
    ax.set_title('Erosion and Accretion by Period', fontsize=16,
fontweight='bold', pad=20)
    ax.set_xticks(x)
    ax.set_xticklabels(df['Period'])
    ax.legend(bbox_to_anchor=(1.05, 1), loc='upper left')
    ax.grid(True, alpha=0.3)
    ax.axhline(y=0, color='black', linewidth=0.8)

    plt.tight_layout()
    plt.show()

def plot_net_change():
    fig, ax = plt.subplots(figsize=(12, 8))

    x = np.arange(len(net_df['Period']))
    width = 0.18
    spacing = 0.26

    for i, zone in enumerate(['Zone 1', 'Zone 2', 'Zone 3']):
        values = net_df[zone]
        color = net_colors[i]
        ax.bar(x + (i - 1) * spacing, values, width, label=zone,
color=color, alpha=0.9)

    ax.set_xlabel('Period', fontsize=12, fontweight='bold')
    ax.set_ylabel('Net Volume Change (m³)', fontsize=12,
fontweight='bold')
    ax.set_title('Net Volume Change by Period', fontsize=16,
fontweight='bold', pad=20)
    ax.set_xticks(x)
    ax.set_xticklabels(net_df['Period'])
    ax.legend()
    ax.grid(True, alpha=0.3)
    ax.axhline(y=0, color='black', linewidth=0.8)

    plt.tight_layout()
    plt.show()

def plot_both():
    fig, (ax1, ax2) = plt.subplots(2, 1, figsize=(14, 12))

    # Erosion/Accretion bars
```

```
    x = np.arange(len(df['Period']))
    width = 0.12
    spacing = 0.18

    ax1.bar(x - 2.5*spacing, df['Zone 1 Erosion'], width,
label='Zone 1 Erosion', color=erosion_colors[0])
    ax1.bar(x - 1.5*spacing, df['Zone 2 Erosion'], width,
label='Zone 2 Erosion', color=erosion_colors[1])
    ax1.bar(x - 0.5*spacing, df['Zone 3 Erosion'], width,
label='Zone 3 Erosion', color=erosion_colors[2])

    ax1.bar(x + 0.5*spacing, df['Zone 1 Accretion'], width,
label='Zone 1 Accretion', color=accretion_colors[0])
    ax1.bar(x + 1.5*spacing, df['Zone 2 Accretion'], width,
label='Zone 2 Accretion', color=accretion_colors[1])
    ax1.bar(x + 2.5*spacing, df['Zone 3 Accretion'], width,
label='Zone 3 Accretion', color=accretion_colors[2])

    ax1.set_xlabel('Period', fontsize=12, fontweight='bold')
    ax1.set_ylabel('Volume Change (m³)', fontsize=12,
fontweight='bold')
    ax1.set_title('Erosion and Accretion by Period',
fontsize=14, fontweight='bold')
    ax1.set_xticks(x)
    ax1.set_xticklabels(df['Period'])
    ax1.legend(loc='upper left')  # Legend now inside the plot
    ax1.grid(True, alpha=0.3)
    ax1.axhline(y=0, color='black', linewidth=0.8)

    # Net Change bars
    x2 = np.arange(len(net_df['Period']))
    width2 = 0.15
    spacing2 = 0.26

    for i, zone in enumerate(['Zone 1', 'Zone 2', 'Zone 3']):
        values = net_df[zone]
        color = net_colors[i]
        ax2.bar(x2 + (i - 1) * spacing2, values, width2,
label=zone, color=color, alpha=0.9)

    ax2.set_xlabel('Period', fontsize=12, fontweight='bold')
    ax2.set_ylabel('Net Volume Change (m³)', fontsize=12,
fontweight='bold')
    ax2.set_title('Net Volume Change by Period', fontsize=14,
fontweight='bold')
    ax2.set_xticks(x2)
    ax2.set_xticklabels(net_df['Period'])
    ax2.legend(loc='upper left')
```

```
    ax2.grid(True, alpha=0.3)
    ax2.axhline(y=0, color='black', linewidth=0.8)

    plt.tight_layout()
    plt.show()


# Example usage
if __name__ == "__main__":
    # plot_erosion_accretion()
    # plot_net_change()
    plot_both()

    print("Erosion/Accretion Data:")
    print(df.to_string(index=False))
    print("\nNet Change Data:")
    print(net_df.to_string(index=False))
```

D2 Depth change

```
import matplotlib.pyplot as plt
import numpy as np
from scipy.interpolate import make_interp_spline

# Data - in chronological order
periods = ['2017-2012', '2020-2017', '2025-2020']
zone1_data = [None, -0.71, -0.73]
zone2_data = [-0.21, -1.01, -0.65]
zone3_data = [0.21, 0.35, -0.91]

# Create x-axis positions for proper chronological ordering
x_positions = [0, 1, 2]

# Create figure and axis
fig, ax = plt.subplots(figsize=(10, 6))

# Plot lines for each zone with smooth curves
# Create smooth curves using spline interpolation
x_smooth = np.linspace(0, 2, 100)

# Zone 1 - starts from second point since first is None
zone1_x = x_positions[1:]
zone1_y = zone1_data[1:]
if len(zone1_x) > 1:
    zone1_spline = make_interp_spline(zone1_x, zone1_y, k=1)  #
k=1 for linear between 2 points
    zone1_smooth = zone1_spline(np.linspace(1, 2, 50))
    ax.plot(np.linspace(1, 2, 50), zone1_smooth,
color='#3584bc', linewidth=2, label='Zone 1')
```

```
    ax.plot(zone1_x, zone1_y, 'o', color='#3584bc',
markersize=8)

# Zone 2 - all points
zone2_spline = make_interp_spline(x_positions, zone2_data, k=2)
# k=2 for quadratic spline
zone2_smooth = zone2_spline(x_smooth)
ax.plot(x_smooth, zone2_smooth, color='#3faa40', linewidth=2,
label='Zone 2')
ax.plot(x_positions, zone2_data, 'o', color='#3faa40',
markersize=8)

# Zone 3 - all points
zone3_spline = make_interp_spline(x_positions, zone3_data, k=2)
# k=2 for quadratic spline
zone3_smooth = zone3_spline(x_smooth)
ax.plot(x_smooth, zone3_smooth, color='#ff983e', linewidth=2,
label='Zone 3')
ax.plot(x_positions, zone3_data, 'o', color='#ff983e',
markersize=8)

# Set x-axis labels
ax.set_xticks(x_positions)
ax.set_xticklabels(periods)

# Customize the plot
ax.set_xlabel('Time Period', fontsize=12)
ax.set_ylabel('Average Depth (m)', fontsize=12)
ax.set_title('Average Depth Changes Over Time', fontsize=14,
fontweight='bold')

# Set y-axis limits to contain all curves
ax.set_ylim(-1.2, 0.5)
ax.set_yticks([-1.05, -0.7, -0.35, 0, 0.35])

# Add grid
ax.grid(True, alpha=0.3)

# Add legend
ax.legend(loc='center right', bbox_to_anchor=(1.0, 0.5))

# Adjust layout
plt.tight_layout()

# Show the plot
plt.show()

# Optional: Save the plot
```

```
# plt.savefig('depth_changes_graph.png', dpi=300,
bbox_inches='tight')
```

D3 Longitudinal profile

```
import pandas as pd
import matplotlib.pyplot as plt

df = pd.read_csv('profile.csv')

layers = {
    'DTM 2012': ('phase2#1_x', 'phase2#1_y'),  # distance,
elevation
    'DTM 2017': ('dtm17#1_x', 'dtm17#1_y'),
    'DTM 2020': ('dtm20#1_x', 'dtm20#1_y'),
    'DTM 2025': ('focaled17#1_x', 'focaled17#1_y'),
}

colors = {
    'DTM 2012': '#f4a261',   # orange
    'DTM 2017': '#cf295b',   # red
    'DTM 2020': '#2ca02c',   # green
    'DTM 2025': '#1f77b4',   # blue
}

plt.figure(figsize=(12, 6))
all_elevations = []

print("Valid points and distance range per layer:")

for label, (dist_col, elev_col) in layers.items():
    if dist_col in df.columns and elev_col in df.columns:
        distance = pd.to_numeric(df[dist_col], errors='coerce')
        elevation = pd.to_numeric(df[elev_col], errors='coerce')

        valid = (~distance.isna()) & (~elevation.isna())
        valid_distance = distance[valid]
        valid_elevation = elevation[valid]

        if valid.sum() > 0:
            print(f"{label}: {valid.sum()} valid points,
distance range: {valid_distance.min()} to
{valid_distance.max()}")
            plt.plot(valid_distance, valid_elevation,
label=label, color=colors[label])
            all_elevations.append(valid_elevation)
        else:
            print(f"{label}: No valid points")
```

```
# Zone lines at distance 259 and 411
for xpos in [259, 411]:
    plt.axvline(x=xpos, color='black', linestyle='dotted',
linewidth=1)

if all_elevations:
    combined_elev = pd.concat(all_elevations)
    y_min = combined_elev.min()
    y_max = combined_elev.max()
    plt.ylim(y_min - 0.1, y_max + 0.1)

    plt.text(150, y_max, 'Zone 1', ha='center', fontsize=10,
color='gray')
    plt.text(335, y_max, 'Zone 2', ha='center', fontsize=10,
color='gray')
    plt.text(450, y_max, 'Zone 3', ha='center', fontsize=10,
color='gray')

plt.xlabel('Distance (m)')
plt.ylabel('Elevation (m)')
plt.title('Longitudinal Profile (2012-2025)')
plt.legend()
plt.grid(True)
plt.tight_layout()
plt.show()
```

D4 Cross section

```
import pandas as pd
import matplotlib.pyplot as plt
import glob

# Define the layers with new column names
layers = {
    'DTM 2012': ('2012#1_x', '2012#1_y'),  # distance, elevation
    'DTM 2017': ('2017#1_x', '2017#1_y'),
    'DTM 2020': ('2020#1_x', '2020#1_y'),
    'DTM 2025': ('2025#1_x', '2025#1_y'),
}

colors = {
    'DTM 2012': '#f4a261',   # orange
    'DTM 2017': '#cf295b',   # red
    'DTM 2020': '#2ca02c',   # green
    'DTM 2025': '#1f77b4',   # blue
}

# Read all CSV files (assuming they have similar structure)
csv_files = glob.glob('cross_3.csv')  # You can specify exact
```

```
filenames if needed
# Alternative: csv_files = ['file1.csv', 'file2.csv',
'file3.csv']

plt.figure(figsize=(12, 6))
all_elevations = []

print("Valid points and distance range per layer:")

for csv_file in csv_files:
    print(f"\nProcessing file: {csv_file}")
    df = pd.read_csv(csv_file)

    for label, (dist_col, elev_col) in layers.items():
        if dist_col in df.columns and elev_col in df.columns:
            distance = pd.to_numeric(df[dist_col],
errors='coerce')
            elevation = pd.to_numeric(df[elev_col],
errors='coerce')

            # Since you mentioned no empty values, we can still
check for any potential issues
            valid = (~distance.isna()) & (~elevation.isna())
            valid_distance = distance[valid]
            valid_elevation = elevation[valid]

            if valid.sum() > 0:
                print(f"{label}: {valid.sum()} valid points,
distance range: {valid_distance.min():.2f} to
{valid_distance.max():.2f}")
                plt.plot(valid_distance, valid_elevation,
label=f"{label}",
                         color=colors[label], alpha=0.8)
                all_elevations.append(valid_elevation)
            else:
                print(f"{label}: No valid points")


if all_elevations:
    combined_elev = pd.concat(all_elevations)
    y_min = combined_elev.min()
    y_max = combined_elev.max()
    y_range = y_max - y_min
    plt.ylim(y_min - 0.1 * y_range, y_max + 0.1 * y_range)

plt.xlabel('Distance (m)')
plt.ylabel('Elevation (m)')
plt.title('Zone 3 Cross Section Profile (2012-2025)')
```

```
plt.legend()
plt.grid(True)
plt.tight_layout()
plt.show()
```

E: Project files

All the raw UAV imagery and LAS format point clouds are stored on server at the Geosciences Airborne Research Facility, file location E:\ARI\00754. Please contact Tom Wade (tom.wade@ed.ac.uk) if access is required.

Project File	**Notes**
M:\dissfinal\UAVdata	Processed L1 and P1 data including DEMs
M:\dissfinal\dod	DoD shp of all periods and datasets
M:\dissfinal\public	Public aerial imagery, historical maps and DTM datasets and processed shp
M:\dissfinal\results_analysis	Rate change analysis, profile analysis and volumetric analysis datasets
M:\dissfinal\output	ArcGIS map package and all the output figures